The Dissertation Committee for Jiaxin Han
certifies that this is the approved version of the following dissertation:

Real-Space Pseudopotential Calculations for the Electronic and Structural Properties of Nanostructures

Committee:

James R. Chelikowsky, Supervisor

Alex Demkov

Allan MacDonald

Brian Korgel

Leonard Kleinman

Real-Space Pseudopotential Calculations for the Electronic and Structural Properties of Nanostructures

by

Jiaxin Han, B.S.

DISSERTATION

Presented to the Faculty of the Graduate School of
The University of Texas at Austin
in Partial Fulfillment
of the Requirements
for the Degree of

DOCTOR OF PHILOSOPHY

THE UNIVERSITY OF TEXAS AT AUSTIN
August 2010

Acknowledgments

First and foremost, I would like to thank my supervisor, Professor James Chelikowsky for his guidance, encouragement and support throughout my graduate study. I have also benefited greatly from his suggestions and creative ways to solve the problems. I owe my sincere thanks to Professor Alex Demkov, Professor Allan MacDonald, Professor Brian Korgel, and Professor Leonard Kleinman, for serving as members of my doctoral committee and for their invaluable suggestions in all my research endeavors. I am indebted to Professor Scott Beckman and Dr. Tzu-Liang Chan, who were post-doctoral fellows in the Chelikowsky lab. Both were always ready and willing to help me with extreme patience during the past several years. I wish them continued success in the future. I would also like to address thanks to the former and current members of the Chelikowsky group for their assistance and advices: Dr. Murilo Tiago, Professor Gustavo Dalpian, Dr. Alexey Zayak, Professor Igor Vasiliev, Dr. Marie Lopez del Puerto, Dr. Na Sai, Dr. Amy Khoo, Dr. Jaehyeon Eom, Dr. Jonathan Moussa, Dr. Lingzhu Kong, Dr. Hyunwook Kwak, Grady Schofield, and Minjung Kim. This work was supported by the National Science Foundation, and the U.S. Department of Energy. I would like to thank the Texas Advanced Computing Center (TACC) and National Energy Research Scientific Computing Center (NERSC) for providing high performance computing resources.

I would like to express my profound gratitude to the faculty in the Department of Physics, especially Professor Takeshi Udagawa, Professor John Keto, Professor Arno Bohm, Professor Herbert Berk, Professor Qian Niu, Professor Ken Shih. In addition, I would like to acknowledge my fellow colleagues and friends in the Department of Physics and Institute for Computational Engineering and Sciences at the University of Texas at Austin. Very special thanks to my wife for her love, care and support. Lastly, I would like to say thanks to my family and friends back in China for their care and encouragement.

Real-Space Pseudopotential Calculations for the Electronic and Structural Properties of Nanostructures

Publication No. ____________________

Jiaxin Han, Ph.D.
The University of Texas at Austin, 2010

Supervisor: James R. Chelikowsky

Nanostructures often possess unique properties, which may lead to the development of new microelectronic and optoelectronic devices. They also provide an opportunity to test fundamental quantum mechanical concepts such as the role of quantum confinement. Considerable effort has been made to understand the electronic and structural properties of nanostructures, but many fundamental issues remain. In this work, the electronic and structural properties of nanostructures are examined using several new computational methods. The effect of dimensional confinement on quantum levels is investigated for hydrogenated Ge $\langle 110 \rangle$ using the plane-wave density-functional-theory pseudopotential method. We present a real-space pseudopotential method for calculating the electronic structure of one-dimensional periodic systems such as nanowires. As an application of this method, we examine H-passivated Si nanowires. The band structure and heat of formation of the Si nanowires are presented and compared to plane wave methods. Our method is able to offer the same accuracy as the traditional plane wave methods, but offers a number of computational advantages such as the ability to handle large systems and a better ease of implementation for highly parallel platforms.

Doping is important to many potential applications of nano-regime semiconductors. A series of first-principles studies are conducted on the P-doped Si $\langle 110 \rangle$ nanowires by the real-space pseudopotential methods. Nanowires of varied sizes and different doping positions are investigated. We calculate the binding energies of P atoms, band gaps of the wires, energetics of P atoms in different doping positions and core-level shift of P atoms. Defect wave functions of P atoms are also analyzed. In addition, we study the electronic properties of phosphorus-doped silicon $\langle 111 \rangle$ nanofilms using the real-space pseudopotential method. Nanofilms with varied sizes and different doping positions are investigated. We calculate the binding energies of P atoms, band gaps of the films, and energetics of P atoms in different doping positions. Quantum confinement effects are compared with P-doped Si nanocrystals and as well as nanowires. We simulate the nanofilm STM images with P defects in varied film depths, and make a comparison with the experimental measurement.

Table of Contents

List of Tables

List of Figures

Chapter 1

General Introduction

Nanoscience is one of the most promising and fast-growing fields in the study of materials physics. Considerable effort has been made in the development of next generation materials for electronic devices within the nano-regime. As a consequence, there is a growing interest in developing devices and related applications based on nanostructures. Progress in the nanowire is exemplified by the construction of high performance Si-nanowire field-effect transistors, logic gates assembled Si-nanowire building blocks and a direct-current nanowire generator driven by ultrasonic wave [3–6]. Nanowire sensors are also potentially employed for highly sensitive and selective detection of biological and chemical species [7, 8].

The properties of nanostructures are strongly dependent on their electronic structure and related properties. Although considerable effort has been make to understand the electronic and structural properties of nanostructures, including experimental and computational work, many fundamental issues remain. My graduate research focuses on a quantitative understanding of the structural and electronic property of materials in the nano-regime such as nanowires and nanofilms, using computational methods based on quantum physics theories.

It is largely accepted that one of the most revolutionary scientific achievements in the history of humankind is the birth of quantum physics. Quantum mechanical laws make it theoretically possible to study the behavior of matter and energy at atomic scales. The birth of quantum physics is attributed to Max Planck's 1900 paper on blackbody radiation; upto the mid-1920's, developments in quantum mechanics quickly made it the standard formulation. Most of the subsequent mathematical developments, interpretations, and improvements were made by a number of distinguished physicists, including Albert Einstein, Niels Bohr, Werner Heisenberg, Erwin Schroedinger, Max Born and Paul Dirac, and many others [9]. In the mid-1920's, the emergence of the Schrödinger wave equation sets the stage for the new physics. It is one of the fundamental equations of quantum mechanics and describes the spatial and temporal behavior of matter. The wave function describes a wave of probability, the square of whose amplitude is equal to the probability of finding a particle at a certain position. The solution of the Schrödinger wave equation is a milestone for an essential complete understanding of the dynamics of matter at the atomic scale [9].

The pseudopotential ideas date back to the 1930's and certainly were understood in the 1950's. In 1934 Fermi introduced a construction to account for the shift in the wave functions of high lying states of alkali atoms subject to perturbations from foreign atoms [10]. In this paper, Fermi introduced the conceptual basis for the pseudopoential. The advent of two key ideas, density functional theory (DFT) and pseudopotentials provided major breakthroughs. Density functional theory is based on transforming the many body problem to a single electron problem. The pseudopotential method replaces the true potential arising from the core states (i.e., chemically inert states and the nuclear charge) by an effective potential that replicates only the valence states (i.e., the chemically active states). This leads to a substantial reduction of computational complexity for our system of interests. Employing the pseudopotential sets the length and energy scales to those of the valence states. In Chapter 2, we will review these two fundamental theories.

In order to explore nanostructures, one must be able to predict the electronic and structural properties of these systems accurately and efficiently. Using the local density approximation pseudopotential method, we can rewrite the Schrödinger equation to Kohn-Sham equation, which can be solved using several different methods. One of them is to use plane-wave basis. However, since a plane wave basis is “infinite” in extent, applying this approach to a localized system can present problems. Typically, for systems with lower dimensionality, a supercell is employed that embeds the system of interest in a large cell. The cell contains a large amount of vacuum space to minimize the interaction between periodic images of the system. This procedure can be very complicated for charged systems or systems with large dipole moments. For such systems, compensating backgrounds are often employed [11, 12].

A different approach to the problem is to solve the electronic structure on a real space grid without an explicit basis set. An advantage of the real space method is its flexibility of imposing different types of boundary conditions for the system of interest. With real space methods, it is possible to use periodic boundary conditions for three dimensional systems as for plane waves [13,14], and equally well consider a confined boundary for clusters or quantum dots [15], or an asymptotic open boundary condition for studying electron transport properties [16]. In Chapter 3, we present a real-space formalism for the electronic structure and total energy calculations for one dimensional periodic systems [17]. Real space algorithms avoid the use of fast Fourier transforms by performing all the calculations in real physical space instead of Fourier space. Unlike fast Fourier transforms, real space methods do not require global communications, and they are efficient for implementation on multi-processor platforms. A large but extremely sparse secular equation will be set up and solved using a sophisticated procedure based on an iterative diagonalization method. The codes for this method had already been developed for localized systems before, but codes for periodic one-dimensional nanowires did not exist before my research work.

In Chapter 4, as an example of using the plane-wave density-functional-theory pseudopotential method, the effect of dimensional confinement on quantum levels has been investigated for hydrogenated Ge $\langle 110 \rangle$ [18]. The limitations of a plane wave method are illustrated, i.e., we need to align the band structures using a reference level to compare wires of different sizes. However, the band structures of different wires can be easily compared using the one-dimensional real space method, as all the eigenvalues are relative to the vacuum level.

In Chapter 5, we present another first-principles study on the hydrogen-passivated Si $\langle 110 \rangle$ nanowires using the real-space pseudopotential methods [17]. We study the band structure and the heat of formation of hydrogen-passivated Si $\langle 110 \rangle$ nanowires using our method, and compare our results with a plane-wave package ABINIT. We show that the results from the two very different methods agree well with each other.

Single crystal P-doped n-type Si nanowires with controlled phosphorus dopant concentrations have been synthesized and used to fabricate field effect transistors, which exhibit good device properties [19]. Highly sensitive, label-free (no isotope label) and multiplexed electrical detection of cancer markers have been successfully made by using P-doped Si nanowire field effect transistor sensor arrays [20]. Although there are some theoretical studies on P-doped Si nanowires [21], several critical and fundamental issues remain unclear, e.g., it is difficult to determine the exact position of the doped atoms.

In Chapter 6, we present a first-principle study of P-doped Si nanowires using the real-space pseudopotential method [13–15, 22, 23]. Nanowires of varied sizes and different doping positions are investigated. We calculate the binding energies of the P atoms, band gaps of the different-sized wires, energetics of the P atoms in different doping positions and core-level shift of the P atoms. Defect wave functions of the P atoms are analyzed. Quantum confinement effects in this one-dimensional periodic system are compared with the P-doped Si nanocrystals.

In Chapter 7, we study the electronic properties of phosphorus-doped silicon $\langle 111 \rangle$ nanofilms using the real-space pseudopotential method. Nanofilms with varied depths and different doping positions are investigated. We also calculate the binding energies of P atoms, band gaps of the films, and energetics of P atoms in different doping positions. Quantum confinement effects are compared with P-doped Si nanocrystals and as well as nanowires. We present simulations for the nanofilm STM images with P defects in different film depths, and make a comparison with the experimental measurement and calculations.

Chapter 2

Theoretical Basis

Several excellent reviews have been written to give an overview of numerical problems encountered when determining the electronic structure of materials and various techniques used to solve the problems [24–26]. In this chapter, I will provide a general overview. It is common knowledge that the behavior of condensed matter is determined by solving the Schrödinger equation, which is very difficult to solve for a system with more than a few electrons. The development of approximation methods has been attempted for several decades. Over the last sixty years, a number of very successful approximations have been made to make a solution of the Schrödinger equation possible, such as Born-Oppenheimer approximation [27], density functional theory [28, 29], and pseudopotential scheme [30]. Over the last thirty years, a number of algorithmic advances have added in the search for the solution to the Schrödinger equation. These advances included a finite difference discretization in real-space [31] and an efficient Chebyshev-filtered subspace iteration method [32, 33].

2.1 Quantum descriptions of matter

The electronic structure of a given condensed matter system can be described by the wave function Ψ that can be acquired by solving the Schrödinger equation:

$$H\Psi = \varepsilon\Psi \tag{2.1}$$

where H is the Hamiltonian operator for the system, ε is the total electronic energy of the system and Ψ is the wavefunction. Considering the essential features of the nanoscale materials and omitting some terms such as those involving relativistic interactions, the Hamiltonian for this system in its simplest form can be written as

$$\begin{aligned} H(\mathbf{R_1}, \mathbf{R_2}, \mathbf{R_3}, ...\mathbf{r_1}, \mathbf{r_2}, \mathbf{r_3}...) = \sum_{n=1}^{N} \frac{-\hbar^2\nabla_n^2}{2M_n} + \frac{1}{2}\sum_{n,m=1,n\neq m}^{N} \frac{Z_n Z_m e^2}{|\mathbf{R_n} - \mathbf{R_m}|}, \\ + \sum_{i=1}^{M} \frac{-\hbar^2\nabla_i^2}{2m} - \sum_{n=1}^{N}\sum_{i=1}^{M} \frac{Z_n e^2}{|\mathbf{R_n} - \mathbf{r_j}|} + \frac{1}{2}\sum_{i,j=1,i\neq j}^{M} \frac{e^2}{|\mathbf{r_i} - \mathbf{r_j}|} \end{aligned} \tag{2.2}$$

M is the mass of the nucleon, ∇^2 is the Laplacian operator, $\hbar$ is the reduced Planck constant, m is the mass of the electron.

2.2 Born-Oppenheimer approximation

Several successful approximations have been made in order to solve the problem, most of which aimed at removing as many "irrelevant" degrees of freedom from the system as possible. The most fundamental approximation which renders the problem more tractable is Born-Oppenheimer approximation or adiabatic approximation [27]. Since the nuclei are considerably more massive than the electrons, it can be assumed that the electrons will respond "instantaneously" to the nuclear coordinates. The Hamiltonian can be rewritten as

$$H(\mathbf{r_1}, \mathbf{r_2}, \mathbf{r_3}, ...) = \sum_{i=1}^{M} \frac{-\hbar^2 \nabla_i^2}{2m} - \sum_{n=1}^{N} \sum_{i=1}^{M} \frac{Z_n e^2}{|\mathbf{R_n} - \mathbf{r_j}|} + \frac{1}{2} \sum_{i,j=1, i \neq j}^{M} \frac{e^2}{|\mathbf{r_i} - \mathbf{r_j}|} \tag{2.3}$$

For most condensed matter systems, the Born-Oppenheimer approximation is highly accurate [34,35].

2.3 Density functional theory

Even with the Born-Oppenheimer approximation, the Schrödinger equation remains difficult to solve. An electron density based approach, which is now known as "density functional theory", was proposed by Hohenberg, Kohn and Sham [28,29]. Although other attempts using density functional theory, e.g. Thomas-Fermi theory, were known before Kohn-Sham, Kohn, Sham and Hohenberg were the first to put this theory on "rigorous" ground. The Hohenberg and Kohn theorem states that for any system of electrons in an external potential V_{ext}, the Hamiltonian is determined only by the ground-state density alone. The ground-state density of a system in a particular external potential can be obtained by minimizing an associated energy functional. For any interacting electron system, with external potential V_{ext}, there is a local potential V_{KS}, resulting a density ρ equal to that of the interacting system. In this framework, the energy functional is generally partitioned into four parts

$$E[\rho] = T[\rho] + \int dr v_{ext}(\mathbf{r})\rho(\mathbf{r}) + \frac{1}{2} \iint d\mathbf{r} d\mathbf{r}' \frac{\rho(\mathbf{r})\rho(\mathbf{r})'}{|\mathbf{r} - \mathbf{r}'|} + E_{XC}[\rho] \tag{2.4}$$

where $T[\rho]$ is the kinetic energy of the system and the next two terms are external potential energy and Hartree energies, respectively. The external potential energy is usually produced by nuclear potential. E_{XC} accounts for the exchange and correlation energies. Here the ion-ion interaction energy is not included in this energy functional form. When performing structure relaxation, the ion-ion interaction energy is added to the total energy to find the optimized geometry.

In principle, the Hohenberg-Kohn theorem aims at constructing the ground-state energy as a functional of the electron density; however, the exact form of $T[\rho]$ and E_{XC} remains unknown. To solve this problem, a non-interacting reference system with a set of independent orbitals ψ_i is set up. We use the atomic units (e=$\hbar$=m=1). The kinetic energy is evaluated as

$$T[\rho] = \sum_{i}^{occ} < \psi_i | -\frac{1}{2} \bigtriangledown^2 | \psi_i > \tag{2.5}$$

The electron density of the real system is equal to that of the reference system and given by the summation of the squared wave functions

$$\rho(\mathbf{r}) = \sum_{i}^{occ} |\psi_i|^2 \tag{2.6}$$

We can apply the variational principle with respect to these orbitals subject to the constraint that the orbitals remain normalized

$$\frac{\delta}{\delta\psi^*} \left\{ E[\rho] - \sum_{j} \varepsilon_j (< \psi_j | \psi_j > -1) \right\} = 0 \tag{2.7}$$

in which ε is the Lagrangian multiplier. Substituting Eqns. 2.4 to 2.6 into 2.7 yields a set of Kohn-Sham single-particle equations

$$\left(-\frac{1}{2}\bigtriangledown^2 + v_{eff}\right)\psi_i = \varepsilon_i\psi_i \tag{2.8}$$

where the effective potential v_{eff} is defined by

$$v_{eff}(\mathbf{r}) = v_{ext}(\mathbf{r}) + \int d\mathbf{r}'\frac{\rho(\mathbf{r}')}{|\mathbf{r}-\mathbf{r}'|} + \frac{\delta E_{XC}[\rho]}{\delta\rho(\mathbf{r})} \tag{2.9}$$

The Kohn-Sham equation can be rewritten as the following for an one-electron potential

$$\left(\frac{-\nabla^2}{2} + V_{KS}\right)\psi(\mathbf{r}) = \varepsilon\psi(\mathbf{r}), \tag{2.10}$$

$$V_{KS} = V_N[r] + V_H[\rho] + V_{XC}[\rho] \tag{2.11}$$

Here $V_N[r]$ is defined as a nuclear potential, which the i th electron sees as

$$V_N(\mathbf{r_i}) = -\sum_{n=1}^{N}\frac{Z_n}{|\mathbf{R_n}-\mathbf{r_i}|} \tag{2.12}$$

$V_H[\rho]$ is the Coulomb or Hartree potential, which is defined by

$$V_H[\rho] = \int \rho(\mathbf{r})\frac{1}{|\mathbf{r}-\mathbf{r}'|}d^3r' \tag{2.13}$$

The exchange-correlation potential in Kohn-Sham equation describes the exchange interaction and the electronic correlation between electrons in the frame of electron density. The exchange-correlation interactions contain the interactions only within the quantum physics framework, for example, Pauli exclusion principle and quantum many-body effect. The exchange energy originates by recognizing two electrons can not be in the same state at the same time. All the remaining interactions are expressed in the correlation term. Several forms for constructing the exchange-correlation functionals have been made, i.e., the generalized gradient approximation (GGA) [36,37], meta-GGA [38] etc. Among them, the local density approximation (LDA) [39] is the simplest. LDA assumes that the electron density can be locally treated as a uniform electron gas. Accordingly, the exchange-correlation energy per electron at a certain position can be calculated from its position and density. Within LDA, the exchange energy is expressed as

$$E_{XC}(\rho(\mathbf{r})) = \int \rho(\mathbf{r})\varepsilon_{XC}\left[\rho(\mathbf{r})\right] d^3\mathbf{r} \tag{2.14}$$

where $\varepsilon_{XC}[\rho]$ is the exchange energy per particle of a uniform gas at a density of ρ. The exchange-correlation energy ε_{XC} is separated into the exchange energy ε_X and the correlation energy ε_C,

$$\varepsilon_{XC} = \varepsilon_X + \varepsilon_C \tag{2.15}$$

The exchange energy is derived to be

$$\varepsilon_X(\rho(\mathbf{r})) = -\frac{3}{4\pi}(3\pi^2\rho(\mathbf{r}))^{1/3} \tag{2.16}$$

The correlation energy ε_C is expressed in terms of the difference between the exact exchange correlation energy and the exchange energy ε_X. Because the form of the exact exchange-correlation functional is unknown, the expression is often parameterized based on the behaviors of small electronic systems. For our work, we employ the Ceperley-Alder functional for the LDA correlation energy [40]. The Perdew-Zunger parameterization [41] of this functional is used, based on two different analytical expressions with respect to the density parameter named the local Seitz radius $r_s = (3/4\pi\rho)^{1/3}$,

$$\varepsilon_C(r_s) = \begin{cases} Alnr_s + B + Cr_s + Xr_s^2lnr_s & \text{if } r_s < 1 \\ \gamma/(1 + \beta_1\sqrt{r}_s + \beta_2 r_s) & \text{if } r_s \geq 1 \end{cases} \tag{2.17}$$

The numerical values of all fitting parameters are listed in Table 2.1.

The Kohn-Sham equation for the electronic structure of matters can be solved using a self-consistent field. An approximate charge is assumed to estimate the exchange-correlation potential and the Hartree potential. After the total charge density solved from the equation, the resulting "output" charge density will be used to construct new exchange-correlation and Hartree potentials. The process continues until the "input" and "output" charge densities are identical to within the tolerance. Once we obtain the solution to the Kohn-Sham equation, the total energy can be calculated from

$$E_{KS} = \sum_i^M E_i - \frac{1}{2}\int \rho(\mathbf{r})V_H(\mathbf{r})d^3\mathbf{r} + \int \rho(\mathbf{r})(E_{XC}\left[\rho(\mathbf{r})\right] - V_{XC}\left[\rho(\mathbf{r})\right])d^3\mathbf{r} \tag{2.18}$$

The electronic energy as determined from E_{KS} must be added to the ion-ion interactions to obtain the structure energies.

2.4 Pseudopotentials

The pseudopotential method along with density functional theory provides a feasible way to compute the electronic properties of materials. The

Parameters	Numerical values
A	0.0311
B	-0.048
C	0.0020
D	-0.0116
γ	-0.1423
β_1	1.0529
β_2	0.3334

Table 2.1: Fitting parameters for the correlation energy formula given by Eqn. 2.17. All values are in atomic units in this chapter (e=$\hbar$=m=1).

pseudopotential approach makes it possible to predict the properties of complex systems such as an atomic cluster or a quantum dot with thousands of atoms. The main idea of pseudopotentials is to remove the core electrons from the subspace considered. Pseudopotentials come in a variety of different forms, which can be computed from "first principles" (ab inito pseudopotentials [22]), or they can be fit to experiment (empirical pseudopotentials [42, 43]).

The Kohn-Sham equation for an atom can be easily solved for the all-electron wave functions and eigenvalues. Using a spherical symmetry for the atom, the atomic wave functions can be written as a product of a radial part and spherical harmonics. The radial wave functions satisfy

$$\left\{-\frac{1}{2}\frac{d^2}{dr^2}+\frac{l(l+1)}{2r^2}+v_{eff}(r)\right\} rR_{nl}(r)=\varepsilon_{nl} rR_{nl}(r) \tag{2.19}$$

where n and l are the principal and angular momentum quantum number, respectively. In general, we calculate no more than one valence state per angular momentum and the index n will be omitted for brevity. The effective potential is given by

$$v_{eff}(r) = -\frac{Z}{r} + v_H[\rho(r)] + v_{XC}[\rho(r)] \tag{2.20}$$

The pseudo-wave functions are constructed from all-electron wave functions. Since the ion cores can be treated as chemically inert and highly localized, the resulting potential produced by the ion core is transferable to other chemical environments. In 1980, Kerker [44] suggested a straightforward method for constructing local density pseudopotentials and there are some certain criteria Kerker proposed for fixing the parameters (a_0, a_1, a_2 and a_3). He suggested that the pseudo wave function have the following form:

For $r < r_c$

$$rR_l^p(r) = r^l exp(p(r)) \tag{2.21}$$

where p(r) is a simple polynomial $p(r) = -a_0r^4 - a_1r^3 - a_2r^2 - a_3$.

For $r > r_c$

$$rR_l^p(r) = \psi_l^{AE}(r) \tag{2.22}$$

In this procedure, there is certain degree of flexibility in introducing the pseudo wave functions with the following criteria satisfied:(1) The wave function is norm conserving. This means that the integral of the pseudo-charge density, i.e., square of the wave function, within the core should be equal to the integral of the all-electron charge density. (2) The all electron and pseudo wave functions have the same valence eigenvalue. (3) The pseudo-wave function should be nodeless and be identical to the all-electron wave function for $r > r_c$, where r_c defines the size spanned by the ion core, i.e., the nucleus and core electrons. Typically, the core is taken to be less than the distance corresponding to the maximum of the valence wave function, but greater than the distance of the outermost node. (4) The pseudo wave function must be continuous as well as the first and second derivatives of the wave function at r_c.

Following the above pseudo wave function, the function will be nodeless and converge to the all-electron wave function at large r.

One can invert the Kohn-Sham equation for the effective potential $v^p_{l,eff}(r)$ corresponding to the pseudo wave function

$$v^p_{l,eff}(r) = \varepsilon^p_l - \frac{l(l+1)}{2r^2} + \frac{1}{2rR^p_l(r)}\frac{d^2}{dr^2}[rR^p_l(r)] \tag{2.23}$$

The potential not only includes the effect of the core part of an atom, but also contains the screening effect of the valence electrons. The Hartree potential $v_H(\rho^p(r))$ and the exchange-correlation potential $v_{XC}(\rho^p(r))$ are computed directly from the pseudo wave function. The ionic potential $v^p_{l,ion}(r)$ is then computed by substracting these potentials from the pseudopotential we constructed,

$$v^p_{l,ion}(r) = v^p_{l,eff}(r) - v_H(\rho^p(r)) - v_{XC}(\rho^p(r)) \tag{2.24}$$

where $\rho^p(r)$ is the pseudo charge density evaluated from the pseudo wave function $rR^p_l(r)$.

There are other methods in the literature for constructing pseudopotentials, e.g., those methods proposed by Hamann, Schluter, and Chiang [45], Bachelet, Hamann, and Schluter [46] and Greenside and Schluter [47]. These pseudopotentials were constructed differently. The all-electron potential was calculated for the free atom. This potential was multiplied by a smooth, short range cut-off function which removes the strongly attractive and singular part of the potential. The cut-off function is adjusted numerically to obtain eigenvalues equal to the all-electron valence eigenvalues, and to yield nodeless wave functions converged to the all electron wave functions outside the core region. The pseudo charge within the core is constrained to be the same as the all-electron value.

The procedure above can be summarized by the following form of Kohn-Sham equation and solve for the ion core pseudopotential $V^n_{ion,p}$

$$V^n_{ion,p}(\mathbf{r}) = E_n - V_H(\mathbf{r}) - V_{XC}[\mathbf{r}, \rho(\mathbf{r})] + \frac{\nabla^2 \phi_{p,n}}{2\phi_{p,n}} \tag{2.25}$$

This potential, screened by the pseudo-charge density based on self-consistent iterations:

$$\rho(\mathbf{r}) = \sum_{n,occup} |\phi_{p,n}(\mathbf{r})|^2 \tag{2.26}$$

yields an eigenvalue of E_n and a pseudo wave function $\phi_{p,n}$. The pseudo wave function by construction agrees with the all electron wave function away from the core.

One important property of the pseudopotential is its non-locality. The pseudopoential of this form is nonlocal in the angular direction, but local in

r. The ionic part of the pseudopotential can be separated into the local term and the non-local term. Although it is more common to treat nonlocality of pseudopotential in the Fourier space, we can also express it in the real space. The interactions between valence electrons and pseudo-ionic cores may be separated into a local potential and a Kleinman and Bylander [48] form of a nonlocal pseudopotential in real space [49].

$$V_{ion}^{p}(\mathbf{r})\phi_n(\mathbf{r}) = \sum_a V_{loc}(|\mathbf{r_a}|)\phi_n(\mathbf{r}) + \sum_{a,n,lm} G_{n,lm}^{a} u_{lm}(\mathbf{r_a})\Delta V_l(\mathbf{r_a}) \tag{2.27}$$

$$G_{n,lm}^{a} = \frac{1}{< \Delta V_{lm}^{a} >} \int u_{lm}(\mathbf{r_a})\Delta V_l(\mathbf{r_a})\psi_n(\mathbf{r})d^3\mathbf{r} \tag{2.28}$$

and $< \Delta V_{lm}^{a} >$ is the normalization factor,

$$< \Delta V_{lm}^{a} >= \int u_{lm}(\mathbf{r_a})\Delta V_l(\mathbf{r_a})u_{lm}(\mathbf{r_a})d^3\mathbf{r} \tag{2.29}$$

where $\mathbf{r_a} = \mathbf{r} - \mathbf{R_a}$, and the u_{lm} are the atomic pseudopotential wave functions of angular momentum quantum numbers (l,m) from which the l-dependent ionic pseudopotential, $V_l(\mathbf{r})$ is generated. $\Delta V_l(\mathbf{r}) = V_l(\mathbf{r}) - V_{loc}(\mathbf{r})$ is the difference between the l component of the ionic pseudopotential and the local ionic potential.

2.5 Real-space finite difference implementation

One of the most successful methods for the pseudopotential-density-functional calculation is to use a plane wave basis expansion. Only valence electrons need to be considered and the resulting pseudopotential converges rapidly compared to the all-electron potential, which makes the plane-wave computation practical. However, for disordered or nonperiodic systems such as clusters, liquids and surfaces, the Bloch's theorem can not be applied directly. Often it makes sense in these situations to reinstate periodicity in an artificial sense such as using supercell geometries. In this method, the system of interest is put in a large cell and the cell is artificially repeated in space. However, this plane-wave-supercell approach might be computationally expensive since the supercell has to be large enough to avoid interactions between neighboring units. The supercell approach also appears to be problematic for charged systems [50, 51]. In the supercell configurations, unless a compensating background charge is added, the Coulomb energy diverges for charged systems.

An alternative approach is to solve the Kohn-Sham equation in real space using higher-order finite difference methods [31]. If we perform a higher order expansions of the Laplacian operator on a uniform grid for the system of interest in three dimensional space, we can write the Kohn-Sham equation as

$$\begin{aligned}\frac{-1}{2}[\sum_{n_1=-N}^{N} c_{n_1}\psi(x_i+n_1h, y_j, z_k) + \sum_{n_2=-N}^{N} c_{n_2}\psi(x_i, y_j+n_2h, z_k)+ \\ \sum_{n_3=-N}^{N} c_{n_3}\psi(x_i, y_j, z_k+n_3)] + [V_{ion}^{p}(x_i, y_j, z_k)+ \\ V_H(x_i, y_j, z_k) + V_{XC}(x_i, y_j, z_k)]\psi(x_i, y_j, z_k) = E\psi(x_i, y_j, z_k)\end{aligned} \tag{2.30}$$

where N is the number of grid points, V_{ion}^{p} is the ionic pseudopotential, V_H is the Hartree potential, and V_{XC} is the local density expression for the exchange and correlation potential. The Hartree and exchange-correlation potentials are locally defined on the grids and the operations on wave functions can be trivial. For the nonlocal ionic pseudopotential, one can use the Kleinman-Bylander separable form in real space

$$V_{ion}^{p}(x,y,z) = V_{loc}(x,y,z)\psi(x,y,z) + \sum_{lm} G_{lm} u_{lm}(x,y,z)\Delta V_l(x,y,z) \tag{2.31}$$

where

$$G_{lm} = \frac{u_{lm}(x,y,z)\Delta V_l(x,y,z)\psi(x,y,z)dxdydz}{u_{lm}(x,y,z)\Delta V_l(x,y,z)u_{lm}(x,y,z)dxdydz} \tag{2.32}$$

Here the integration can be evaluated by summing over the grid points. If there are N grid points, the size of the full matrix will be N × N.

2.6 Solving the eigenvalue problem

The most computationally expensive part of the DFT calculation is solving for the eigenvalues, i.e., diagonalizing the matrix. In order to solve this problem more efficiently, a recently proposed nonlinear Chebyshev-filtered subspace interaction (CheFSI) method has been developed by Zhou et al [32, 33]. In this approach, only the initial iteration requires solving an eigenvalue problem. This step is employed to provide a good initial subspace (or good initial approximation to the wave functions). Because the subspace dimension is slightly larger than the number of wanted eigenvalues, the method does not require as much memory as standard restarted eigensolvers.

The main idea of this method is to start with a good initial eigen-basis, ψ_n, corresponding to occupied states of the initial Hamiltonian, and then to improve adaptively the subspace by polynomial filtering. At a given self-consistent step, a Chebyshev polynomial filter C_m, of order m is constructed for the current Hamiltonian H. As the eigen-basis is updated, the Chebyshev polynomial will be different at each SCF step since H will change. The goal of the filter is to make the subspace spanned by $\psi'_n = C_m(H)\psi_n$ approximate the eigen subspace corresponding to the occupied states of H. There is no need to make the new subspace, ψ'_n, approximate the wanted eigen subspace of H to high accuracy at intermediate steps. Instead, the filtering is designed so that the new subspace obtained at each self-consistent iteration step will progressively approximate the wanted eigen subspace of the final Hamiltonian when self-consistency is reached. All that is required to obtain a good filter at a given SCF step, is to provide a lower bound and an upper bound of an interval of the spectrum of the current Hamiltonian H. The lower bound can be readily obtained from the values computed from the previous step, and the upper bound can be inexpensively obtained by a very small number of steps. Hence the main cost of the filtering at each iteration is in computing the polynomial operation.

The filtering procedure [32] for the self-consistent cycle is illustrated in Fig.2.1. Unlike traditional methods, the cycle only requires one explicit diagonalization step. Instead of repeating this step again within the self-consistent loop, a filtering operation is used to create a new basis in which the desired eigen subspace is enhanced. After the new basis, $\left\{\psi'_i\right\}$, is formed, the basis is orthogonalized. The orthogonalization step scales as the cube of the number of occupied states and as such this method is not an "order-n" method. However, the prefactor is sufficiently small that the method is much faster than previous implementations of real space methods. The cycle is repeated until the "input"and "output" density is unchanged.

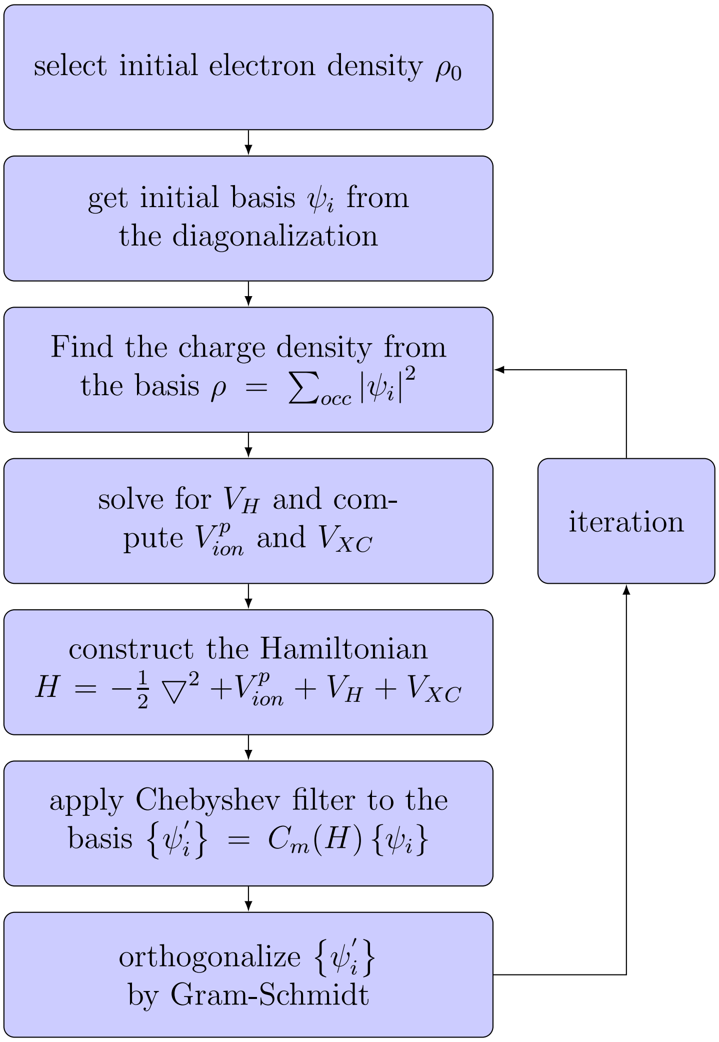

Figure 2.1: Algorithmic flow chart for a self-consistent field calculation using CheFSI method.

Chapter 3

Real-space Methods for Solving the Kohn-Sham Problem in One-Dimensional Periodic Systems

One of the approaches to solve the electronic structure problem is to use a real space grid without an explicit basis set. There are many advantages in using the real space method over a plane wave method. With a real space method, it is easy to impose different types of boundary conditions for the system of interest. Real space methods can be applied to systems with periodic boundary conditions, or systems with a confined boundary for clusters or quantum dots [15], or an asymptotic open boundary condition for studying electron transport properties [16]. Since a plane wave basis is "infinite" in extent, dealing with a charged and localized system based on plane wave can be very complicated. The derivation of using a real space pseudopotential method for calculating the electronic structure of one-dimensional periodic systems is illustrated in this section [17]. As a demonstration, we will apply the methodology to study hydrogen-passivated Si nanowires, which is presented in Chapter 5.

3.1 The one-dimensional periodic Kohn-Sham problem

The electronic structure of a one-dimensional periodic system can be obtained by solving the Kohn-Sham equation [28, 29]:

$$\left(\frac{-\hbar^2\nabla^2}{2m} + V_{ion}[\mathbf{r}] + V_H[\rho] + V_{XC}[\rho]\right)\psi_{n,k}(\mathbf{r}) = \varepsilon_{n,k}\psi_{n,k}(\mathbf{r}), \tag{3.1}$$

where V_{ion} is the ion-core pseudopotential, V_H is the Hartree potential, and V_{XC} is the exchange-correlation potential, as a functional of the ground state electron density ρ. The eigenstate $\psi_{n,k}(\mathbf{r}) = exp(ikx)u_{n,k}(\mathbf{r})$ is required to satisfy the Bloch theorem along the x direction and vanish on the boundary of the cylindrical domain. The exchange-correlation functional from Ceperley and Alder [40] are used.

We consider a system periodic in the x direction with a period of a and spatially confined in the y and z directions. A cylindrical domain with radius, L is chosen to enclose such system. L is chosen to be sufficiently large enough so that this requirement does not affect the electronic structure of the system of interest.

$$\left\{\frac{\hbar^2}{2m}\left(-\bigtriangledown^2 + \frac{2}{i}k\frac{\partial}{\partial x} + k^2\right) + V_{ion}[\mathbf{r}] + V_H[\rho] + V_{XC}[\rho]\right\}u_{n,k}(\mathbf{r}) = \varepsilon_{n,k}u_{n,k}(\mathbf{r}) \tag{3.2}$$

with the boundary condition that $u_{n,k}(\mathbf{r})$ has a periodicity of a along the x direction and vanishes on the boundary of the cylindrical domain.

The Kohn-Sham equation is solved self-consistently; summing over k and the occupied states, the electron density ρ is obtained from

$$\rho\left(\mathbf{r}\right) = \sum_{k} \sum_{n=1}^{occ} \mid \psi_{n,k}\left(\mathbf{r}\right) \mid^{2} . \tag{3.3}$$

The ion core pseudopotential [22, 23] in the Kleinman-Bylander form [48]:

$$\begin{aligned} V_{ion} &= \sum_{t=-\infty}^{\infty} \sum_{i=1}^{N} v_{ion}^{i}(\mathbf{r} - \mathbf{R_i} - ta\hat{\mathbf{x}}), \\ v_{ion}^{i}(\mathbf{r}) &= v_{local}^{i}(\mathbf{r}) + \sum_{l \neq local, m} \frac{|\delta v_{l}^{i} \phi_{lm}^{i} >< \delta v_{l}^{i} \phi_{lm}^{i}|}{< \phi_{lm}^{i} | \delta v_{l}^{i} | \phi_{lm}^{i} >}, \end{aligned} \tag{3.4}$$

This form separates the ionic pseudopotential with the non-local part references to a local potential. Here, t labels the periodic images along the wire axis, i refers to the basis in the unit cell with a total number of N atoms, $\mathbf{R_i}$ is the position of the i-th atom and lm are the angular and azimuthal quantum numbers. One of the angular momentum channel l is chosen, typically by convenience, to be the local part of the pseudopotential. $\delta v_{l}^{i} = v_{l}^{i} - v_{local}^{i}$ and $|\phi_{lm}^{i} >$ is the pseudo wave function of the i-th atom with angular momentum lm. $v_{l}^{i}(\mathbf{r}) \to -Z_{i}e^{2}/r$ is independent of l outside of the ion core, where Z_i is the ionic charge of the i-th atom. Consequently, $\delta v_{l}^{i}(\mathbf{r})$ is short-ranged, whereas $v_{local}^{i}(\mathbf{r})$ is Coulombic asymptotically.

The sum of v_{ion}^{i} over all the periodic images in Eqn. 3.4 is divergent owing to $v_{local}^{i}(\mathbf{r})$ [52]. Because the total electrostatic energy of a periodic system is finite when it is electrically neutral, the divergence in v_{ion}^{i} is canceled by the Hartree potential V_H. A compensating charge is added to the local part of the pseudopotential with a corresponding charge subtracted away from the

Hartree potential in the Kohn-Sham equation. In this case, V_{ion} and V_H can be calculated independently and without further complication.

The compensating charges are taken to be a set of Gaussian charge distributions centered on each atomic position:

$$\begin{aligned} \rho_{com}(\mathbf{r}) &= \sum_{t=-\infty}^{\infty} \sum_{i=1}^{N} \rho_{com}^{i}(\mathbf{r} - \mathbf{R_i} - ta\hat{\mathbf{x}}) \\ \rho_{com}^{i}(\mathbf{r}) &= \frac{-Z_i}{(\sqrt{\pi}\sigma_i)^3} exp\left(- \left(\frac{|\mathbf{r}|}{\sigma_i} \right)^2 \right) \end{aligned} \tag{3.5}$$

resulting in the following potential to be added to the local part of V_{ion}:

$$\begin{aligned} V_{com}\left(\mathbf{r}\right) &= \sum_{t=-\infty}^{\infty} \sum_{i=1}^{N} v_{com}^{i}(\mathbf{r} - \mathbf{R_i} - ta\hat{\mathbf{x}}) \\ v_{com}^{i}(\mathbf{r}) &= -\frac{-Z_i e^2}{|\mathbf{r}|}\ erf\left(\frac{|\mathbf{r}|}{\sqrt{2}\sigma_i} \right). \end{aligned} \tag{3.6}$$

σ_i is the width of the Gaussian distribution, and is chosen to be half of the cutoff radius of the pseudopotential of the i-th atom. This choice makes the compensating potential scales approximately as $Z_i e^2/r$ beyond the cutoff radius. Since the compensated ion core potential is short-ranged, only a small number of periodic images($|t|$ ∼3-4) is needed to calculate $V_{ion} + V_{com}$.

The compensated Hartree potential V_H can be calculated from the electronic charge density using the Poisson equation:

$$\begin{aligned} \nabla^2 V_H\left(\mathbf{r}\right) &= \nabla^2 (V_H^0 - V_{com}) \\ &= -4\pi e^2 (\rho\left(\mathbf{r}\right) + \rho_{com}(\mathbf{r})) \end{aligned} \tag{3.7}$$

We solve the Poisson equation by conjugate-gradient minimization with the boundary condition specified using a multipole expansion in cylindrical coordinates [53]:

$$V_H\left(r_\perp = L, \phi, x\right) = Re\left[\sum_{m=-\infty}^{\infty}\sum_{p=-\infty}^{\infty} V_{m,p}(\phi, x)\right] \tag{3.8}$$

$$V_{m,p}(\phi, x) = \frac{2e}{a} q_{m,p} exp(\frac{i2\pi px}{a}) K_m\left(\frac{2\pi p}{a}L\right) exp(im\phi) \tag{3.9}$$

$$q_{m,p} = \int exp(-\frac{i2\pi px}{a}) exp(-im\phi) I_m\left(\frac{2\pi p}{a}r_\perp\right) e(\rho\left(\mathbf{r}\right) - \rho_{com}(\mathbf{r})) d^3\mathbf{r} \tag{3.10}$$

I_m and K_m are modified Bessel functions of the first and second kind respectively, $(r_\perp, \phi, x)$ are the cylindrical coordinates, and $q_{m,p}$ are the multipoles with $V_{m,p}$ the corresponding electrostatic potential. In general, only a few multipoles are needed to calculate the Hartree potential accurately. We note that for $p = 0$, the $K_m\left(\frac{2\pi p}{a}L\right)$ diverges. However, if $m \neq 0$, $I_m\left(\frac{2\pi p}{a}r_\perp\right)$ tends to zero, then $V_{m,0} = \frac{2e^2}{a} exp(im\phi) \frac{1}{2|m|R^{|m|}} \int exp(-im\phi) r_\perp^{|m|} (\rho\left(\mathbf{r}\right) - \rho_{com}(\mathbf{r})) d^3\mathbf{r}$ is finite. The monopole term($m = n = 0$) is zero because the total charge is zero. After calculating the ionic potential V_{ion} and the Hartree potential V_H on a real space grid within the cylindrical domain, we can solve the Kohn-Sham equation(Eqn. 3.1) by using a high order finite differencing method to evaluate the Laplacian and the gradient of the wave functions [54–56] as implemented in the PARSEC code [57].

3.2 Evaluation of total energy and forces

The total energy within density functional theory can be expressed by

$$E_{total} = \sum_k \sum_{n=1}^{occ} \varepsilon_n - \frac{1}{2} E_H + \int \rho\left(\mathbf{r}\right)\left(\varepsilon_{XC}\left[\rho\left(\mathbf{r}\right)\right] - V_{XC}\left[\rho\left(\mathbf{r}\right)\right]\right) d^3\mathbf{r} + E_{ion}, \tag{3.11}$$

where $E_H = \int V_H^0(\mathbf{r})\,\rho(\mathbf{r})\,d^3\mathbf{r}$ is the Hartree energy, E_{ion} is the Coulomb interaction energy between the ions, ε_{XC} is the exchange-correlation energy density.

For the Hartree energy E_H, the evaluation of the Hartree potential V_H^0 is similar to Eqns. 3.7 – 3.10 in the previous section, except the compensating charge distribution is absent. As a result, there is a monopole term in the Hartree potential

$$V_{0,0} = \frac{2e^2}{a} Z(\lim_{2\pi p \to 0} K_0\left(\frac{2\pi p}{a} L\right)) = \frac{2e^2}{a} Z\left[\ln 2 - \gamma - \ln\frac{L}{a} - (\lim_{2\pi p \to 0} \ln(2\pi p))\right]$$

where K is a modified bessel function [58], Z is the total number of electrons in the unit cell and γ is the Euler constant. Consequently, there is a logarithmic divergence in the Hartree energy of the form

$$\frac{-2(Ze)^2}{a}\left(\lim_{2\pi p \to 0} \ln(2\pi p)\right)$$

We will show later that a logarithmic divergence of the same form (but with opposite sign), can be found in the ion-ion interaction energy E_{ion}.

$$\begin{aligned} E_{ion} &= e^2 \sum_{i,j \leq i}^{N} E_{ion}^{i,j}, \\ \text{where } E_{ion}^{i,j} &= \sum_t{}' \frac{Z_i Z_j}{|\mathbf{R_i} - \mathbf{R_j} - ta\hat{\mathbf{x}}|}. \end{aligned} \tag{3.12}$$

$E_{ion}^{i,j}$ is the Coulomb interaction between atom i and all the periodic images of atom j. The prime in the summation in $E_{ion}^{i,j}$ indicates that the $t = 0$ term will be omitted when $i = j$. Since the Coulomb interaction is long-ranged, the summation in $E_{ion}^{i,j}$ diverges. However, if the Coulomb interaction is replaced by a screened Coulomb potential with a screening strength β, the summation can be carried out analytically [59]:

$$
\begin{aligned}
E_{ion}^{i,j} &= \lim_{\beta\to 0} {\sum_t}' \frac{Z_i Z_j exp(-\beta|\mathbf{R_i} - \mathbf{R_j} - ta\hat{\mathbf{x}}|)}{|\mathbf{R_i} - \mathbf{R_j} - ta\hat{\mathbf{x}}|} \\
&= \begin{cases} \frac{4Z_iZ_j}{a}[\sum_{p=1}^{\infty} K_0\left(\frac{2\pi p}{a}|r_{i\perp} - r_{j\perp}|\right)\cos\left(\frac{2\pi p}{a}(x_j - x_i)\right) \\ \qquad + \frac{1}{2}\ln\left(\frac{2a}{|r_{i\perp} - r_{j\perp}|}\right) - \frac{\gamma}{2} - \lim_{a\beta\to 0}\frac{1}{2}\ln(a\beta)] \text{ if } i \neq j \\ \frac{4Z_iZ_j}{a}\left[-\lim_{a\beta\to 0}\frac{1}{4}\ln(a\beta)\right] \text{ if } i = j \end{cases}
\end{aligned}
\tag{3.13}
$$

The true Coulomb interaction can be recovered by taking the limit β to zero. The ion-ion energy E_{ion} has a divergence of the form

$$
\frac{-(Ze)^2}{a}\lim_{a\beta\to 0}\ln(a\beta).
$$

For an electrically neutral system, the logarithmic divergence between the Hartree energy E_H and the ion-ion energy E_{ion} cancels exactly. The total energy can be evaluated via Eqn. 3.11 and dropping the logarithmic divergent term in the monopole of E_H and in E_{ion}. The logarithmic divergence in one-dimensional periodic systems should be contrasted with the three-dimensional periodic ones, in which the divergence behaves like $\lim_{G\to 0} 1/G^2$ [60].

The total force on atom i can be obtained by

$$
\begin{aligned}
\mathbf{F^i} &= -\nabla_{\mathbf{R_i}} E_{total} \\
&= -\sum_k \sum_{n=1}^{occ(k)} < \psi_{n,k}|\nabla_{\mathbf{R_i}} H|\psi_{n,k} > -\nabla_{\mathbf{R_i}} E_{ion},
\end{aligned}
\tag{3.14}
$$

in which we applied the Hellmann-Feynman theorem and used the fact that the Hartree energy calculated from V_H^0 and the exchange-correlation do not explicitly depends on atomic positions. First, we consider the Hellmann-Feynman force. Since Gaussian compensating charges are added to the Kohn-Sham equation, there is an additional force from the local part of the pseudopotential and the Hartree potential now explicitly depends on atomic positions. Note that the compensating charges are just a convenience for numerical computation, they do not produce any physical force to the system. The force on atom i due to the local part of the pseudopotential is

$$\mathbf{F^i_{local}} = \sum_{t=-\infty}^{\infty} - \int \rho(\mathbf{r}) \nabla_{\mathbf{R_i}} \left[\left(v^i_{local} + v^i_{com} \right) \left(|\mathbf{r} - \mathbf{R_i} - ta\hat{\mathbf{x}}| \right) \right] d^3\mathbf{r} \tag{3.15}$$

In practice, only a few periodic images are necessary in the summation. We note $\mathbf{F^i_{local}}$ is convergent without the use of compensating Gaussian charges; however, fewer periodic images are needed to achieve convergence when Gaussian charges are added. The non-local part of the pseudopotential is non-zero only within the cutoff radius of the pseudopotential, *i.e.*, it is short-ranged and its contribution to the force can be evaluated in a similar way as in Ref. [13,14].

For the Hartree potential V_H in the Kohn-Sham equation, only V_{com} depends explicitly on atomic positions. Therefore, the Hellmann-Feynman force from the Hartree potential is

$$\begin{aligned} \mathbf{F^i_H} &= \int \rho(\mathbf{r}) \nabla_{\mathbf{R_i}} V_{com}(\mathbf{r}) d^3\mathbf{r} \\ &= - \int \rho^i_{com}(\mathbf{r}) \nabla_{\mathbf{r}} V_H^0(\mathbf{r} + \mathbf{R_i}) d^3\mathbf{r} \end{aligned} \tag{3.16}$$

where the second line follows from rewriting the V_{com} into a integral form by Coulomb's Law and then exchanging the order of integration.

The ionic Coulomb force on atom i is $\mathbf{F^i_{ion}} = e^2 \sum_{j\neq i}^{N} \mathbf{F^{i,j}_{ion}}$. The periodic images of atom i do not exert net force on itself, and by taking the derivative of Eqn. 3.13 with respect to the atomic position, the ionic Coulomb force on atom i by atom j is found to be

$$\begin{aligned}
\left(F^{i,j}_{ion}\right)_x &= \frac{4Z_iZ_j}{a}\left[\sum_{p=1}^{\infty} K_0\left(\frac{2\pi p}{a}|r_{i\perp} - r_{j\perp}|\right)\frac{2\pi p}{a}\sin\left(\frac{2\pi p}{a}(x_i - x_j)\right)\right] \\
\left(F^{i,j}_{ion}\right)_y &= \frac{4Z_iZ_j}{a}\left[\frac{1}{2|r_{i\perp} - r_{j\perp}|} + \sum_{p=1}^{\infty} K_1\left(\frac{2\pi p}{a}|r_{i\perp} - r_{j\perp}|\right)\frac{2\pi p}{a}\cos\left(\frac{2\pi p}{a}(x_i - x_j)\right)\right] \\
&\frac{(y_i - y_j)}{|r_{i\perp} - r_{j\perp}|} \\
\left(F^{i,j}_{ion}\right)_z &= \frac{4Z_iZ_j}{a}\left[\frac{1}{2|r_{i\perp} - r_{j\perp}|} + \sum_{p=1}^{\infty} K_1\left(\frac{2\pi p}{a}|r_{i\perp} - r_{j\perp}|\right)\frac{2\pi p}{a}\cos\left(\frac{2\pi p}{a}(x_i - x_j)\right)\right] \\
&\frac{(z_i - z_j)}{|r_{i\perp} - r_{j\perp}|}
\end{aligned} \tag{3.17}$$

where (x_i, y_i, z_i) and $(r_{i\perp}, \theta_i, x_i)$ are the Cartesian and cylindrical coordinates of the atomic position $\mathbf{R_i}$ respectively.

When two atoms have the same radial coordinates, i.e. $r_{i\perp} = r_{j\perp}$, there are apparent divergences in the ion-ion energy $E^{i,j}_{ion}$ and the force $F^{i,j}_{ion}$. However, the divergences in Eqn. 3.13 and 3.17 are alternating in sign and a finite number will be obtained by summing the infinite series. When $r_{i\perp} - r_{j\perp} = 0$, Eqn. 3.13 can be recast into a more convenient form for numerical computation

$$E_{ion}^{i,j} = \lim_{\eta\to\infty} \frac{4Z_iZ_j}{a}\left[\sum_{p=1}^{\infty}\frac{1}{2}E_1\left(\left(\frac{p\pi}{a\eta}\right)^2\right)\cos\left(\frac{2\pi p}{a}(x_i - x_j)\right) + \frac{1}{2}\ln\left(2a\eta\right) - \frac{\gamma}{4}\right], \tag{3.18}$$

where E_1 is the exponential integral function and the logarithmic divergent term is dropped from the equation. In practice, a large number($\sim$ 10000) chosen for η can give an accurate evaluation of the energy. In such a case, $\left(F_{ion}^{i,j}\right)_{y,z} = 0$ by symmetry, and the ionic force on atom i by atom j is only non-zero along the x-direction given by

$$\left(F_{ion}^{i,j}\right)_x = \lim_{\eta\to\infty} \frac{4Z_iZ_j}{a}\left[\sum_{p=1}^{\infty}\frac{1}{2}E_1\left(\left(\frac{p\pi}{a\eta}\right)^2\right)\frac{2\pi p}{a}\sin\left(\frac{2\pi p}{a}(x_i - x_j)\right)\right] \tag{3.19}$$

Chapter 4

Quantum Confinement Properties of the Ge $\langle 110 \rangle$ Nanowires

4.1 Introduction and calculation details

It is well-known that quantum confinement strongly affects the optical properties of nanostructures [61–63]. Experimentally much work has been performed studying the optical properties of these nanowires. Although measurements of the photoluminescence spectra of free standing, Si nanowires have been produced [64], little progress has been made in the study of the optical properties of Ge nanowires. It is believed that states at the Ge - Ge oxide interface as well as states from metal contaminates provide numerous sites for non-radiative recombination events. Recent attempts for the photoluminescence spectra measurement from free standing Ge wires grown on Si substrates have resulted in spectra originating from the Ge-Si interface, not the Ge wires themselves [65]. Other studies of the optical properties of Ge nanowires have focused on non-free standing structures. The photoluminescence spectrum has been observed for 1D-structures grown along the edge of steps on a Si substrate [66]. The examined structure has a highly anisotropic (1:10 ratio) cross-section. Other studies have measured the photoluminescence spectra of Ge wires confined to the pores of hexagonal mesoporous silica [67].

The investigation of the optical properties of Ge nanowires can be aided by computational methods. Numerous computational studies have been performed to investigate the optical properties of nanocrystals [68–71]. Similar studies have focused on the absorption spectra of Si nanowires [72]. Preliminary investigations of Ge nanowires are available in the literature [73, 74]. These studies have employed all-electron potentials [73] and the GW corrections [74], have focused exclusively on small-diameter wires.

In this chapter, the effects of confinement on $\langle 110 \rangle$ Ge nanowires will be investigated, using "density functional theory-pseudopotential" methods [18]. Wires with diameters as large as 2.8 nm will be examined. The band structure of different wires as a function of size will be determined, and the role of quantum confinement will be explored.

This work will set a good example for the comparison of methodologies between the plane wave and real space method. In the plane wave method, we have to align the band structures using a reference level to compare wires of different sizes. The band structures of different wires can be easily compared using the one-dimensional real space method, as all the eigenvalues are relative to the vacuum level. In this work, the density functional theory pseudopotential method used here is encoded in ABINIT [39, 75]. The exchange and correlation functional is treated within the local density approximation [40, 76]. The wave function is expressed as a plane wave summation truncated at an energy cutoff of 19 a.u. (atomic units with $e = \hbar = m = 1$, energy units of Hartree, and length unit is Bohr).

For Ge, a Troullier-Martins pseudopotential form is used with $4s^2 4p^2 4d^0$ valence and radial cut-off of $\mathrm{r}_s/\mathrm{r}_p/\mathrm{r}_d = 2.6/2.5/2.8$ a.u. [49]. Partial core correlations are included with a core cut-off of 1.98 a.u. [77]. The pseudopotential is transformed into local and non-local components by the Kleinman-Bylander transformation with the p channel selected as the local component [48]. This pseudopotential predicts a cubic lattice parameter, a_{cubic} of 10.62 a.u., which is within 0.7% of the experimental value of 10.70 a.u. [78]. The elasticity parameters are calculated to be (in GPa) $c_{11} = 129.4$, $c_{12} = 49.98$, and $c_{44} = 67.62$, which is accurate to within 5% of the experimental values $c_{11} = 129.2 \pm 1.2$, $c_{12} = 47.9 \pm 1.2$, and $c_{44} = 67.0 \pm 0.7$ [79].

4.2 Electronic structures of Ge nanowire

Using this pseudopotential, the electronic structure of bulk Ge is calculated and presented in Fig. 4.1. Although it is known that the local density approximation underestimates band gaps, at least to a qualitative level the structure is correct. In particular, the relative ordering of the L, Γ, and X conduction band minima (CBM) is correct [42].

The difference between the highest occupied molecular orbital and lowest unoccupied molecular orbital (the HOMO-LUMO gap) for bulk Ge, is predicted to be 0.44 eV. This corresponds to the transition from the Γ point valence bands maximum (VBM) to the CBM at L. The Kohn-Sham eigenvalues $\mathrm{E}(\mathbf{k})$ are calculated across the entire Brillouin zone and projected into the $\mathbf{k} = \langle 110 \rangle$ direction to produce the projected band structure, shown in Fig.

4.2. In the limit that a $\langle 110 \rangle$ wire's diameter approaches infinity the electronic structure will approach this bulk projected structure. It is apparent in Fig. 4.2 that when projected into the $\langle 110 \rangle$ direction the Ge band-gap is direct, unlike in the bulk crystal. This is because the CBM at L ($\langle \bar{1}11 \rangle$, $\langle 1\bar{1}1 \rangle$, $\langle \bar{1}1\bar{1} \rangle$, $\langle 1\bar{1}\bar{1} \rangle$) maps onto Γ. The CBM is degenerate because the L minima at ($\langle 111 \rangle$, $\langle \bar{1}\bar{1}1 \rangle$,$\langle 11\bar{1} \rangle$, $\langle \bar{1}\bar{1}\bar{1} \rangle$) project to the Brillouin zone edge. For wires smaller than 3 nm, confinement effects increase the energy of the conduction bands at the Brillouin zone edge, leaving only one CBM, at Γ. For wires with diameters larger than 3 nm, the double minima is an important feature in the band structure.

The geometries of the Ge wires investigated are shown in Fig. 4.3. The diameter is taken to be the average dimension of the parallelogram's diagonals, which are (in nm) 0.47, 1.37, and 2.8 for the three wires studied. This cross-sectional shape is chosen to maximize the area of low energy $\langle 111 \rangle$ surfaces; however, it is believed that wires with diameter larger than 1.5 nm prefer a hexagonal shape [80, 81]. The wire shape chosen for this study may not be optimal, but it is known that the band structures for these parallelogram shaped wires are similar to those calculated for hexagonal wires [82]. There is an uncertainty in identifying the cross-sectional diameters of the structures. For the wires in Fig. 4.3(d), (b), and (a), the cross-sectional diameters range (in nm) from 0.34 to 0.42, 1.1 to 1.6, and 2.1 to 3.2, respectively. We propose that the diagonal measure of the wire is a good approximation because it is the largest dimension that will produce the narrowest features of the band edges.

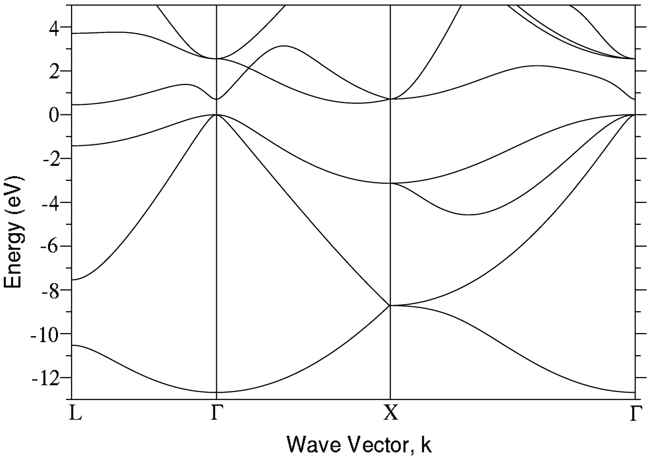

Figure 4.1: The band structure of Ge calculated within pseudopotential density functional theory. The energy zero is taken to be the valence band maximum (VBM). The appearance of the band gap is due to the fact that the LDA pseudopotentials used here do not include the relativistic corrections.

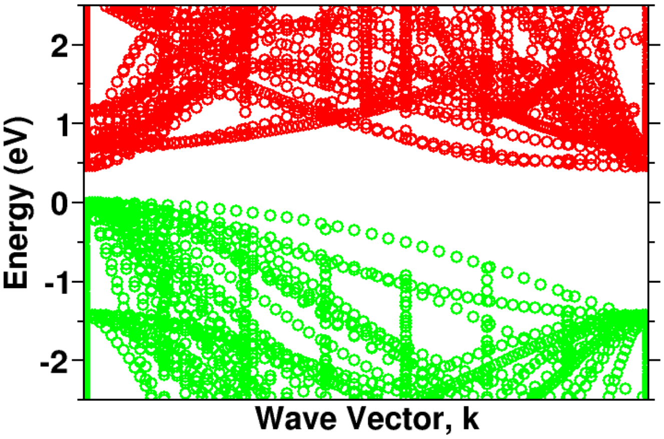

Figure 4.2: The band structure of Ge projected in the ⟨110⟩ direction, from the Brillouin zone center to the Brillouin zone edge.

Confinement in the $\langle\bar{1}\bar{1}2\rangle$ and $\langle 111\rangle$ directions will produce features inside the band. A region of at least 12.2 a.u. of vacuum buffers the wires in neighboring cells, in the x and y directions. The translational periodicity along the wires, in the z direction, is $\frac{\sqrt{2}}{2}a_{cubic}$. Sampling three unique points in the k_z direction is sufficient for total energy convergence to better than 1 meV.

The positions of the atoms are selected according to the lattice parameter calculated for bulk Ge. The surfaces are passivated with hydrogen positioned to eliminate surfaces states in the gap. Hence, the calculations predict the effect of confinement on the HOMO-LUMO gap, while suppressing surface effects. To examine the influence of internal structural relaxation, the two smallest wires are fully relaxed, shown in Fig. 4.3 (c) and (e). Only atoms within one atomic layer of the surface are observed to move and the most pronounced changes are at the corners of the parallelograms. Comparison of the relaxed and unrelaxed electronic structures reveals a change in the HOMO-LUMO gap of 290 meV for the smallest wire and 50 meV change for the 1.37 nm wire (relaxed structures have larger band gaps). The $E(\mathbf{k_z})$ dispersions for the 0.47 nm wires are plotted in Fig. 4.4. Qualitatively the shape of the band edges does not change, yet individual bands are observed to shift. We find internal relaxation for wires larger than 1.3 nm to be negligible.

In addition to identifying the HOMO-LUMO gap in these wires, it is also desirable to align the bands in the different wires. We increase the vacuum region by 12.5 a.u. in the x direction and a hydrogen molecule is placed between the wires, as shown in Fig. 4.5. The molecule is aligned in the y direction with

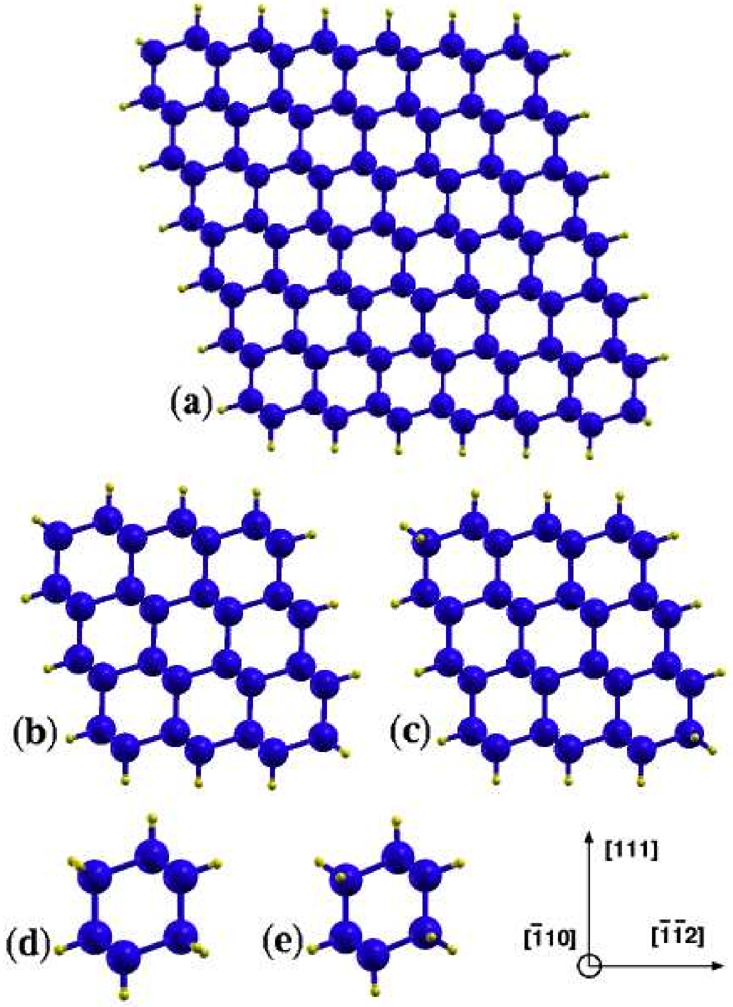

Figure 4.3: The cross sections of the ⟨110⟩ Ge wires studied: (a) 2.8 nm diameter (b) 1.37 nm diameter (c) 1.37 nm diameter with full internal relaxation (d) 0.47 nm diameter (e) 0.47 nm diameter with full internal relaxation.

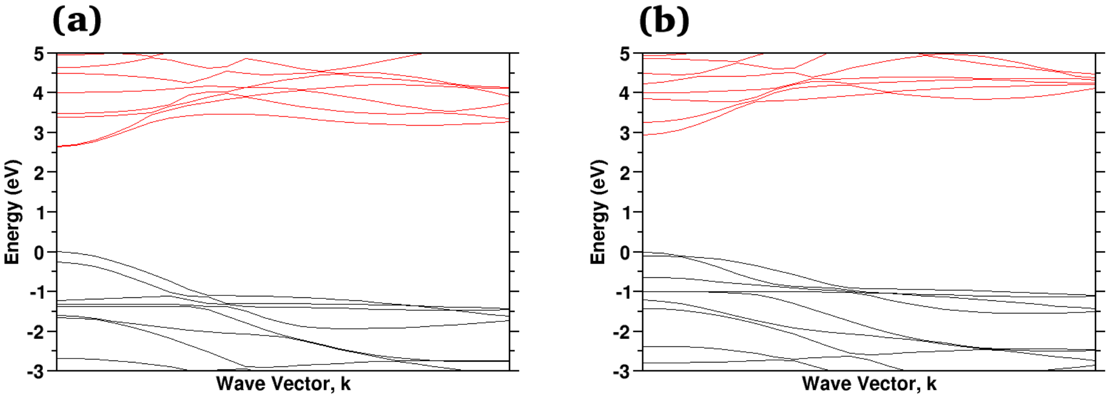

Figure 4.4: The E($\mathbf{k}$) dispersion for the 0.47 nm diameter wires. The energy zero is taken to be the valence band maximum (VBM): (a) the band structure calculated by holding the Ge fixed according to the bulk crystal structure; (b) bands calculated when the entire wire structure is allowed to relax to minimize the total energy.

a bond length of 1.5 a.u. The energy dispersion in the k_z direction for an isolated H_2 molecule in a periodic cell with dimensions $15.0 \times 17.0 \times 7.5066$ a.u. is shown in Fig. 4.6. We find that the states are flat and nearly molecular; the H_2 molecular levels are a good reference for aligning the bands. Because all of the wires have the same period in the z direction, any interaction between the hydrogen molecules does not need to be considered.

The dispersion in the k_z direction for the three wires is plotted in Fig. 4.7. As the diameter increases, the gap decreases, and approaches the predicted bulk band gap. The band edges becomes significantly more bulk-like as the diameter increases. At a diameter of 2.8 nm, the conduction bands at the Brillouin zone edge are almost level with the bands at Γ as predicted for the bulk like bands in Fig. 4.1. The 1.37-nm and 2.8-nm wires have the same VBM. For Ge nanowires with diameters greater than 1.4 nm, the change in the HOMO-LUMO gap is due entirely to the confinement of the CB states. This is consistent with the CB states being inherently less localized than those of the VB.

Within a simple "particle in a box" model, it is predicted that as the diameter, D, is changed, the band gap will vary as $\frac{1}{D^2}$. The calculated highest occupied molecular orbital-lowest unoccupied molecular orbital (HOMO-LUMO) gap versus the diameter is fit to the function

$$E_{gap}(D) = \frac{\alpha}{D^{\beta}} + 0.44 \tag{4.1}$$

with $\alpha = 1.20$ and $\beta = 0.98$ as is shown in Fig. 4.8. In this figure, the Bruno

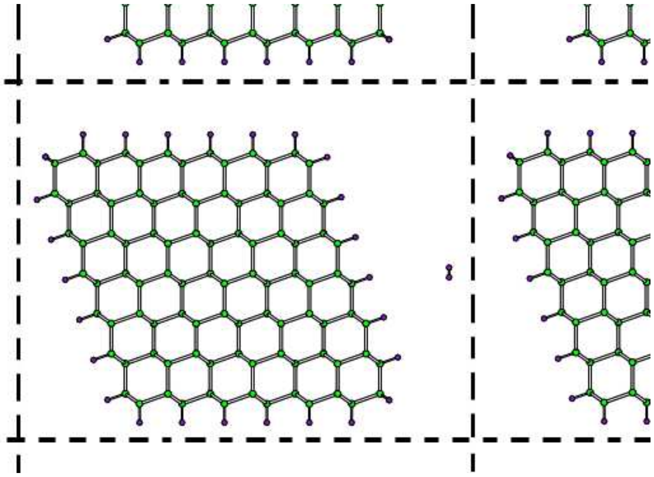

Figure 4.5: The geometry of the supercell with an H_2 molecule to be used as reference. The dashed lines are the boundaries between the neighboring cells. The distance between the surfaces of wires in neighboring cells and the H_2 is 12.5 a.u.

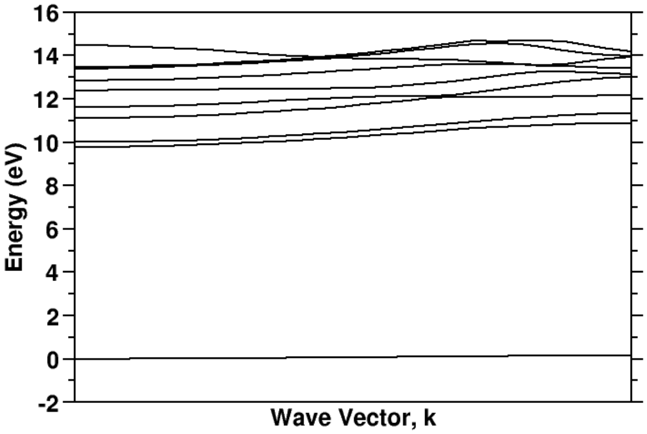

Figure 4.6: The band structure in the k_z direction of an isolated H_2 molecule. The z dimension of the computational cell is selected to have the same periodicity as the Ge ⟨110⟩ wires.

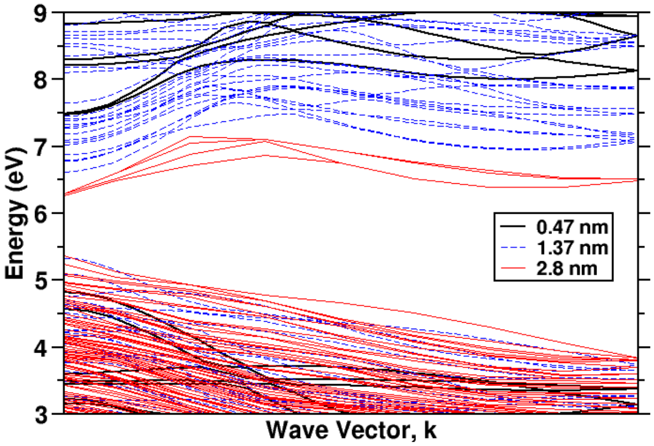

Figure 4.7: The Kohn-Sham E(**k**) dispersions for the three wires with different radius.

data comes from reference [74] and the Kholod data comes from reference [73].

In bulk insulating crystals the self-energy correction to the Kohn-Sham eigenstates, solved for within the GW approximation, results in a rigid shift of the bands, effectively opening the band gap to near the experimentally predicted gap [83]. For the work here, such a rigid shift would leave the coefficients α and β unaffected. The effect of confinement on the corrections due to many-body interactions cannot be known a priori. It is observed in Si nanowires that confinement results in a larger self-energy correction in smaller-diameter wires [67]. One might postulate that if the GW correction were applied to the results in this paper, a small increase in the value of α, and possibly β, would be observed.

Comparison to these previous work indicates the same relative trends. The agreement between the Kholod *et al.* [73], all-electron calculation and the present, for the smallest diameter wire, gives us confidence that the pseudopotential approach is as expected. The slight divergence between the previous study [73] and the present, at larger diameters, can possibly be explained by the difference in wire cross-section, or by the difference between the pseudopotential and all-electron potentials.

In summary, the energy dispersion for hydrogen passivated $\langle 110 \rangle$ Ge nanowires of different diameters is calculated. Atomic relaxations only occur near the surface of the wire, and do not significantly affect the energy bands of wires with diameter greater than 1.3 nm. The HOMO-LUMO gap versus the wire diameter is fit to an appropriate function to allow for the extrapolation of these results to larger diameter wires. The shape of the band edges become bulk-like for wires with diameters greater than 2 nm. The CBM becomes two-fold degenerate, as predicted from the bulk projected bands, for wires with diameter greater than around 3 nm. The effect of confinement on the CBM and VBM is distinguished by using the molecular levels of H_2 as reference. Confinement only significantly affects the VBM for wires with diameters less than around 2 nm.

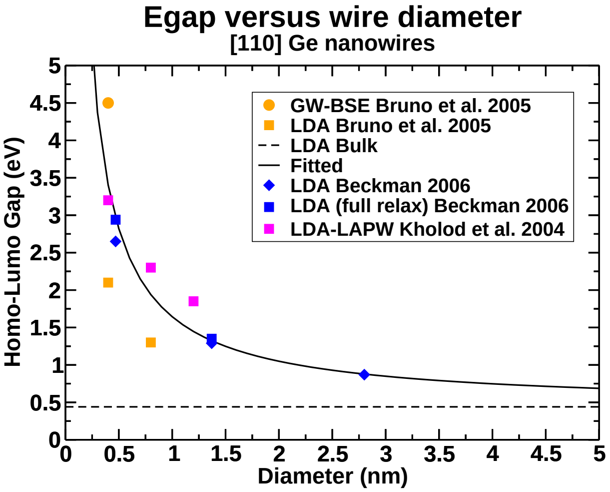

Figure 4.8: A plot of the calculated highest occupied molecular orbital-lowest unoccupied molecular orbital gap versus the wire diameter. The solid line is fit to the data calculated by us.

Chapter 5

Quantum Confinement Effects and Properties in H-passivated Si and InP $\langle 110 \rangle$ Nanowires

5.1 Introduction and calculation details

We present the calculation of the band structure of a hydrogen-passivated Si nanowire [17] using the one-dimensional real space method. The nanowire of interest is a bulk Si fragment with a periodicity of 3.84 Å along the $\langle 110 \rangle$ direction, which equals to the experimental lattice constant of the bulk. We compared our results using real-space method with the plane wave code ABINIT [75].

Our nanowire consists of a unit cell along the axis containing of 16 Si atoms with the Si dangling bonds on the surface passivated by 12 H atoms. The nanowire cross sections are illustrated in Fig. 5.1. The calculated band structures are shown in Fig. 5.2, and the two calculations based on two different methodology are almost identical. The band structure shows that the Si $\langle 110 \rangle$ nanowire has a direct energy gap at Γ. We also consider Si nanowires with diameters from 1.2 nm to 4.3 nm. We define the diameter of a H-passivated Si nanowire to be the smallest cylindrical domain that can enclose the nanowire. The number of Si atoms in a unit cell ranges up to 250 atoms, details of these

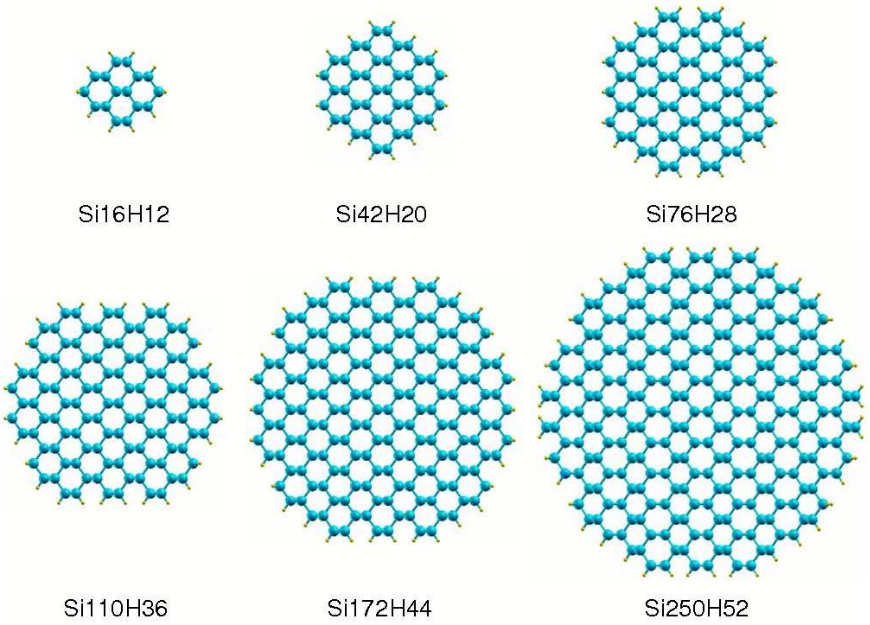

Figure 5.1: The cross sections of H-passivated Si ⟨110⟩ nanowires. The larger spheres correspond to Si atoms, and the smaller ones on the surface of the nanowires are H atoms.

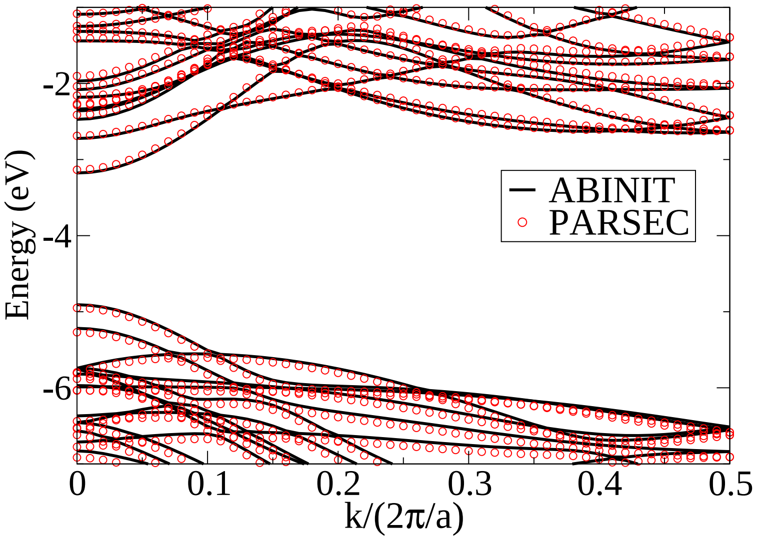

Figure 5.2: The electronic band structure around the band gap for a H-passivated Si ⟨110⟩ nanowire containing 16 Si atoms and 12 H atoms. Results from a real-space (PARSEC) and a plane-wave (ABINIT) codes are shown. For PARSEC, the energy reference is the vacuum level. The middle of the band gap of ABINIT is aligned to that of PARSEC.

n_{Si}	n_H	Radius R(nm)
16	12	0.6
42	20	0.9
76	28	1.2
110	36	1.4
172	44	1.8
250	52	2.1

Table 5.1: The number of Si and H atoms in a unit cell and the radius of six different sizes of H-passivated Si ⟨110⟩ nanowires.

wires are shown in Table 5.1.

Again, we compare our real space results with PARSEC to plane wave results using ABINIT. Both calculations use Troullier-Martins pseudopotentials [84] for Si and H. The PARSEC calculation uses a grid spacing of 0.52 a.u. with 10 a.u. of vacuum space; the ABINIT calculation uses a plane wave cutoff comparable to this grid spacing, *i.e.*, a plane wave cut off of 33 Ry with 20 a.u. (1 a.u.=0.529 Å) of vacuum space between the periodic images. Both calculation use a uniform k-point grid with 8 k-points to sample the Brillouin zone and obtain the charge density.

5.2 Local density approximation band gap of the Si ⟨110⟩ nanowires

Fig. 5.3 illustrates the evolution of LDA energy band gap E_G as a function of nanowire radius. The energy gap increases as nanowire radius decreases owing to quantum confinement and consistent with previous studies

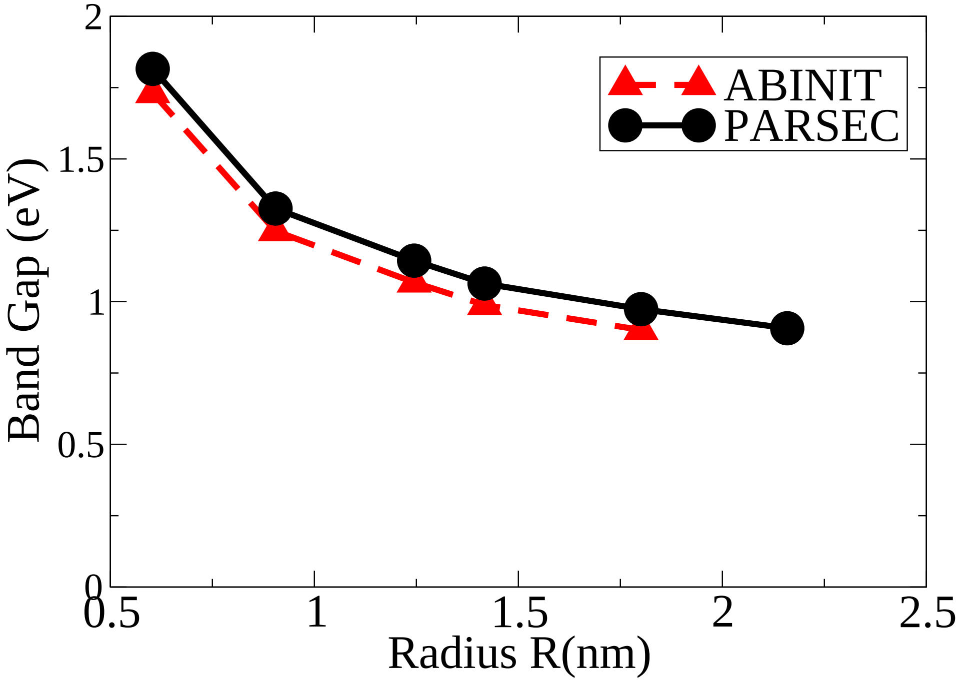

Figure 5.3: The evolution of the band gap of H-passivated Si $\langle 110 \rangle$ nanowires with nanowire radius.

[85]. The results from ABINIT are also shown in the figure. PARSEC and ABINIT agree to within ~0.1 eV, with the ABINIT code yielding a smaller gap. The discrepancy between the two approaches results is likely due to the technical differences in spacial resolution (grid spacing or cut-off in kinetic energy) and different boundary conditions. In particular, cell-cell interactions within the plane wave method tend to converge slowly. These interactions are absent in the real space approach.

The change in the energy gap with the wire radius can be fitted to a power law $\sim 1/R^{1.4}$. The scaling is softer than what is expected from an infinite quantum well model($1/R^2$). A similar behavior has also been observed in previous work for Si and Ge nanowires [18, 85].

In Fig. 5.4, we plot the valence band maximum(VBM) and conduction band minimum(CBM) as a function of the nanowire radius. As radius decreases, the VBM decreases while CBM increases. They exhibit different scaling: VBM$\sim 1/R^{1.2}$ and CBM$\sim 1/R^{1.7}$. Both VBM and CBM are strongly influenced by confinement when the radius of the nanowire is less than 2 nm, such phenomenon has been reported for Ge nanowires as well [18]. The more delocalized nature of the CBM wave functions is consistent with this trend.

5.3 Heat of formation of the Si $\langle 110 \rangle$ nanowires

We also calculated the heat of formation of the Si $\langle 110 \rangle$ nanowires. The heat of formation per Si atom is defined as

$$E_F = \frac{1}{n_{Si}} \left(E_{total} - n_{Si}\mu_{Si} - n_H \mu_H \right), \tag{5.1}$$

where E_{total} is the total energy of the nanowire calculated using Eqn. 3.11, n_{Si} and n_H are the number of the Si and H atoms in a unit cell respectively, μ_{Si} and μ_H are their chemical potentials. In this calculation, μ_{Si} is taken to be the total energy of a Si atom in the bulk while μ_H is chosen to be the total energy of a H_2 molecule per H atom. By definition, the heat of formation measures the energy obtained by creating a Si nanowire from bulk crystalline Si and H_2 molecules.

The heat of formation for forming nanowires are shown in Fig. 5.5,

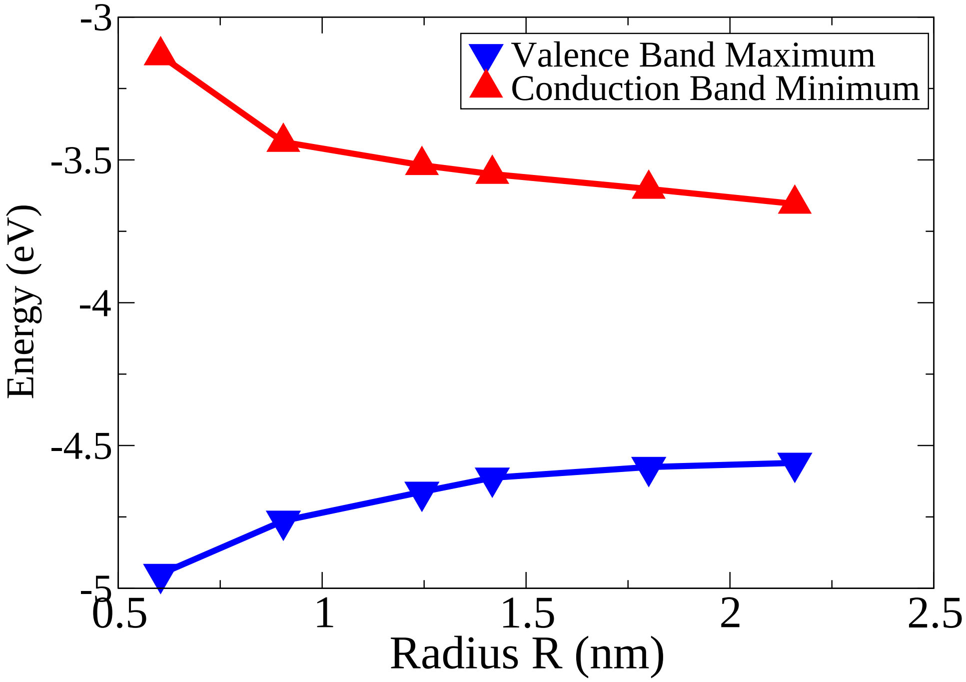

Figure 5.4: The valence band maxima and conduction band minima of H-passivated Si ⟨110⟩ nanowires plotted as a function of nanowire radius. The energy reference is the vacuum level.

together with the results from ABINIT and PARSEC. The two codes agree to within ~ 0.01 eV. As radius increases, the heat of formation trends to zero as expected since the Si nanowire assumes a crystalline silicon configuration. E_F can be fitted to a power law, and it is found to have a scaling of $\sim 1/R$. Since n_{Si} changes with radius as R^2, $(E_{total} - n_{Si}\mu_{Si} - n_H\mu_H)$ scales like R. The numerator in Eqn. 5.1 is a measure of the surface area of the nanowire, and the energetics is dominated by the surface area alone. In Fig. 5.5, we also show the heat of formation after the Si nanowires are relaxed till the force on each atom is less than 0.0015 Ryd/a.u. The nanowires are found to lower their

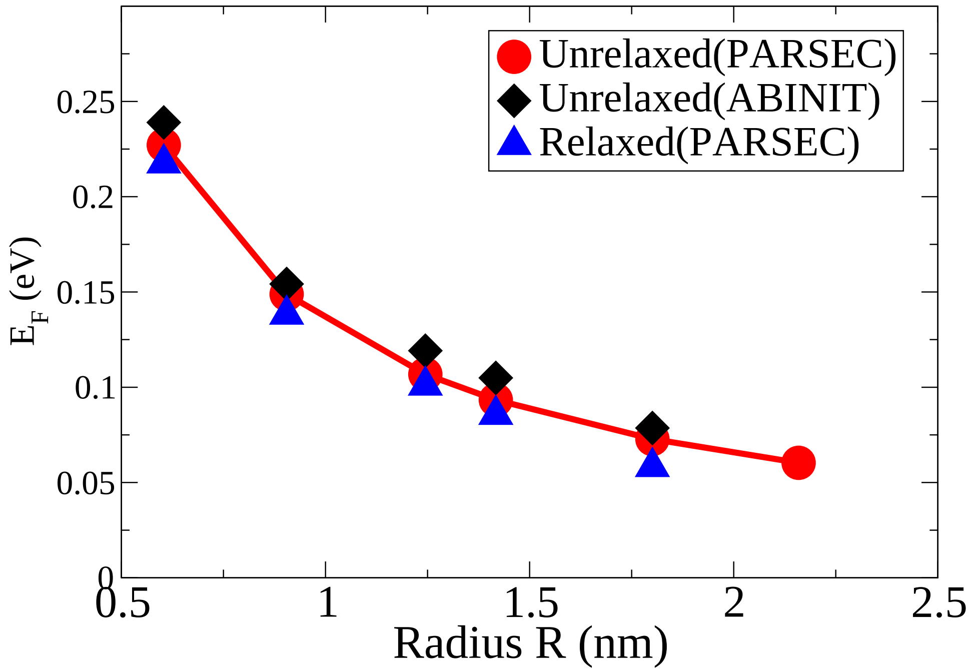

Figure 5.5: A plot of the heat of formation of H-passivated Si ⟨110⟩ nanowires against nanowire radius.

energies by contracting the Si-Si bond close to the surface.

5.4 InP ⟨110⟩ nanowires

In addition to silicon wires, we have also examined some issues with compound or heteropolar wires. This demonstrates that our one-dimensional real space method converges very rapidly with respect to the unit cell volume compare to the plane-wave method, when there is significant dipole moment along the confined direction. Fig. 5.6 depicts an unpassivated InP ⟨110⟩ nanowire, which consists of 21 In and P atoms in a unit cell respectively. The periodicity of the nanowire corresponds to the bulk InP lattice constant of 5.87 Å. The $\langle 111 \rangle$ facets consist of either In or P atoms. These opposite facets will give rise to a significant dipole moment. We calculated the self-consistent potential V_{SCF} for this system and the result is plotted in Fig. 5.6. We used a grid spacing of 0.56 a.u., a vacuum space of 4 Å, and a uniform k-point grid with 16 k-points to sample the Brillouin zone. With the wire axis oriented along the x direction, the self-consistent potential is averaged in the $x - y$ plane and plotted along the z direction.

The self-consistent potential exhibits different values on the opposite sides of the enclosing cylindrical domain owing to the dipole moment. The total energy displayed Fig. 5.7 converges very rapidly with respect to the unit cell volume when confined boundary conditions are imposed on the non-periodic directions. A modest amount of vacuum space($\sim$ 4 Å) is sufficient to converge the total energy. However, a supercell approach with three-dimensional periodic boundary condition using ABINIT converges much more slowly and requires a unit cell nearly twice as large to converge the total energy owing to the long-ranged dipole-dipole interaction between the nanowire facets. Although this situation is a bit unrealistic and one does not expect such a configuration in nature, it does illustrate the advantages that exist for real space descriptions.

In summary, we presented a real-space first-principles formalism for studying the electronic structures of one-dimensional periodic systems such as nanowires. In our formalism, the system of interest need not be embedded

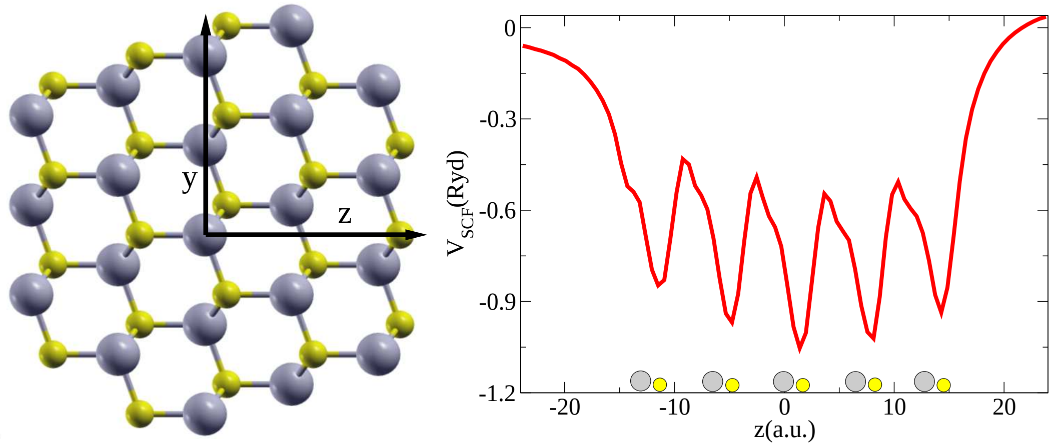

Figure 5.6: Left: The cross section of an InP $\langle 110 \rangle$ nanowire with 21 In(grey) and 21 P(yellow) atoms in a unit cell. Right: A plot of a planar average of the self-consistent potential across the cylindrical domain enclosing the InP nanowire. The gray circles label the position of the In atoms, and the smaller yellow circles for the P atoms.

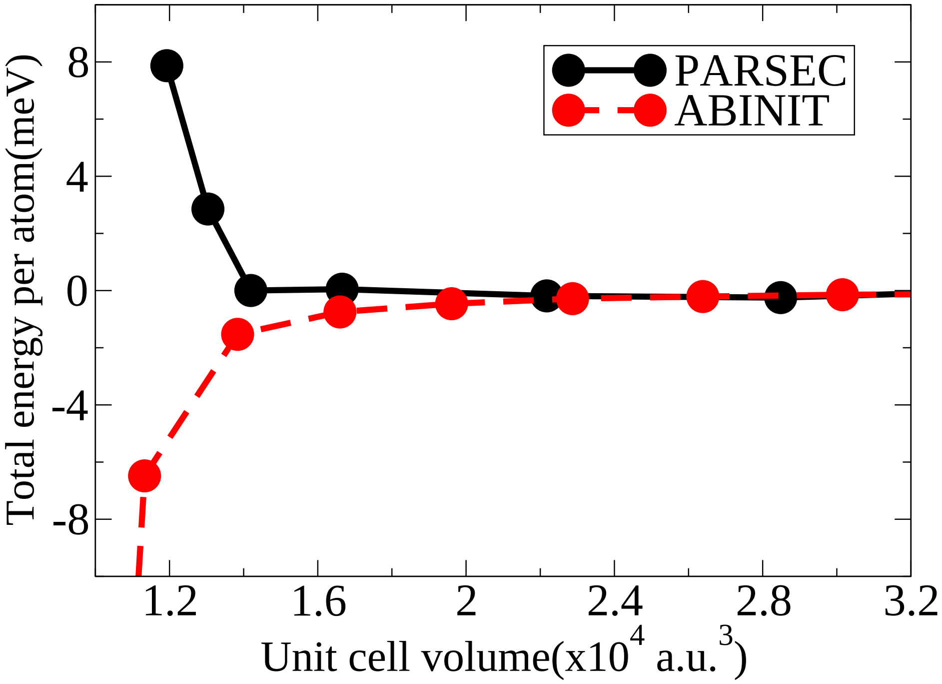

Figure 5.7: The convergence of the total energy of an InP ⟨110⟩ nanowire with respect to unit cell volume.

in a supercell as for calculations using a plane waves basis. Instead, confined boundary conditions are imposed perpendicular to the wire axis. The divergence from the long-range Coulomb behavior of the ionic and Hartree potential in the Kohn-Sham equation is logarithmic for one-dimensional periodic systems. The divergence can be addressed by introducing compensating Gaussian charges into the system. The Kohn-Sham equation is then solved on a real-space grid using high order finite differencing method as implemented in PARSEC.

We studied the band structure and the heat of formation of hydrogen-passivated Si ⟨110⟩ nanowires using our method, and compared our results with a plane-wave package ABINIT. The results from the two very different methods agree well with each other. The band structures of Si ⟨110⟩ nanowires show that there is a direct band gap at Γ. We studied the evolution of the energy gap, conduction band minimum and valance band maximum with nanowire radius. We found strong quantum confinement in these quantities. In addition, the calculated heat of formation of the Si ⟨110⟩ nanowires shows that the surface energy has a strong contribution to the energetics. Through InP ⟨110⟩nanowires, we illustrated that confined boundary conditions imposed on the two non-periodic directions can eliminate interaction between periodic images, which can be significant for systems that exhibit long-range interaction.

Chapter 6

Quantum Confinement Effects and Properties in P-doped Si $\langle 110 \rangle$ Nanowires

The electronic properties of semiconductors can be adjusted when impurities or dopants with more valence electrons than the host species result in n-type doping. Dopants with fewer valence electrons than the host species result in p-type doping. Once the semiconductors were doped, their optical properties or mechanical properties can be changed as well. Experimentally, single crystal P-doped n-type Si nanowires with controlled phosphorus dopant concentrations have been synthesized and used to fabricate field effect transistors, which exhibit good device properties [19, 20]. There are also some theoretical studies about P-doped Si nanowires [21]. A goal of this dissertation is to explore how the properties of doped nano semiconductors vary with size.

6.1 Introduction and calculation details

The cross sections of Si $\langle 110 \rangle$ nanowires are illustrated in Fig. 6.1. The number of atoms and the radius of wires are listed in Table. 6.1. Troullier-Martins pseudopotentials [84] and the PARSEC package [13–15, 17, 23] are

n_{Si}	n_H	Radius R(nm)
14	12	1.1
38	20	1.8
74	28	2.6
122	36	3.3
182	44	4.1
254	52	4.9

Table 6.1: The number of Si and H atoms in a unit cell and the radius of six different sizes of P-doped Si $\langle 110 \rangle$ nanowires.

used in the calculations within the local spin density approximation (LSDA), which describes the role of spin explicitly by considering the charge density for up and down spins [86]:

$$\rho = \rho_{up} + \rho_{down} \tag{6.1}$$

Because the P-doped Si wires have one electron that is not paired, we need to employ an LSDA description.

6.2 Binding energies and band gaps of P atoms

The binding energies of P atoms in Si nanowires are calculated while the P atoms are in the center of the wires. We use 6 smallest cells along the wire axis and 8 a.u. vacuum along the radial direction as super cell. There is only one P atom in the super cell. Only Γ point is calculated. We use 0.6 a.u. as grid spacing. The binding energies of P atoms is the difference of two energy levels: the first is the lowest unoccupied electronic state in pure Si nanowire, and the second is the defect electronic state which is the highest occupied electronic state in P-doped Si nanowire. The band gaps are the gaps in pure Si nanowires. The binding energies and band gaps of different-sized Si nanowire are shown in Fig. 6.2.

The binding energies and band gaps evolve to the bulk limits, 0.046 eV and 0.64 eV respectively. Both curves can be fitted to simple functions of diameters. The band gap of bulk Si is 1.11 eV from experimental measurement [87]. The experimental value for binding energy of P atoms in Si bulk is 0.044 eV [88].

6.3 Energetics

The energetics of P atoms of different doping positions in different-sized Si nanowires are studied. We use 4 smallest cells along wire axis and 8 a.u. vacuum in radial direction as supper cell to relax all the P-doped Si nanowires to their local energy minimum structures. There is only one P atom in the super cell. Only Γ point is calculated. We use 0.4 a.u. as grid spacing. The results of energetics of P atoms are shown in Fig. 6.3. The P atom is more stable on the surface than in the center of the Si nanowires and the center is another stable position when diameter is bigger than 20 Å. The similar results have been found for P-doped Si nano crystals [89]. After annealing process, the doped P atom is expected to stay on the surface of the wires or in the center of the large wires.

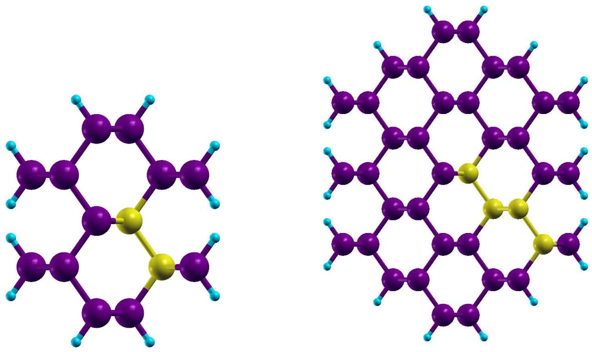

(a) diameter 11 Å (b) diameter 18 Å

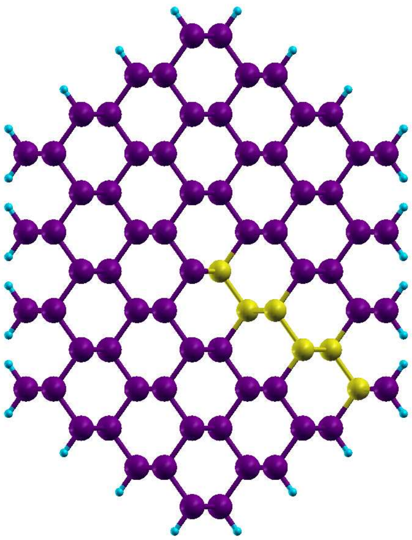

(c) diameter 26 Å

Figure 6.1: The cross sections of H-passivated Si $\langle 110 \rangle$ nanowire, with diameter 11 Å, 18 Åand 26 Å. The purple spheres correspond to Si atoms, and the blue ones on the surface of the nanowires are H atoms. The yellow ones are the doping positions of P atoms.

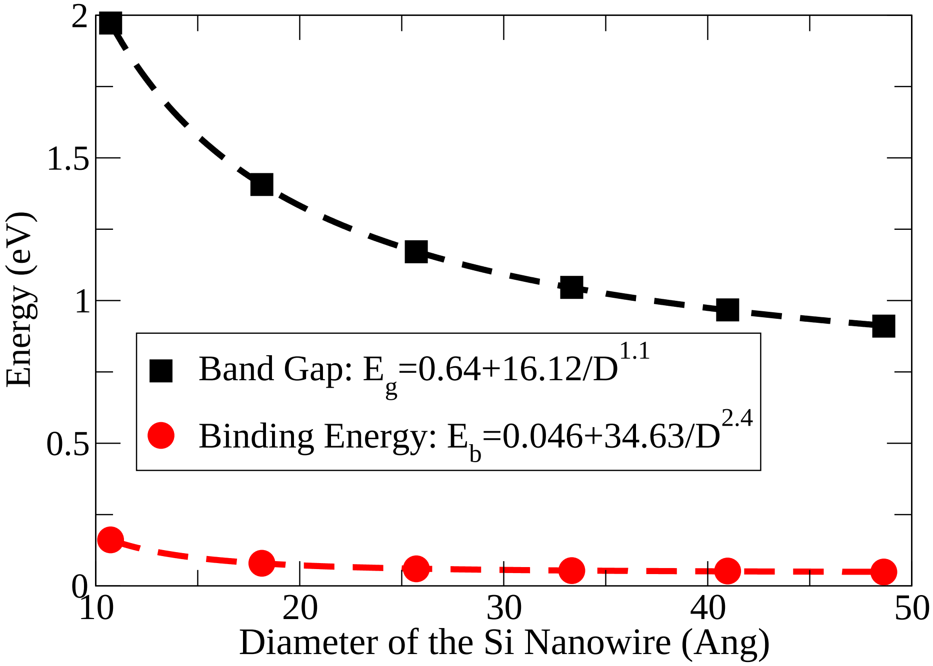

Figure 6.2: Binding energy of P atoms in P-doped Si ⟨110⟩ nanowires. The black curve is band gap for pure Si nanowire. The red curve is binding energy of P atom in Si nanowire.

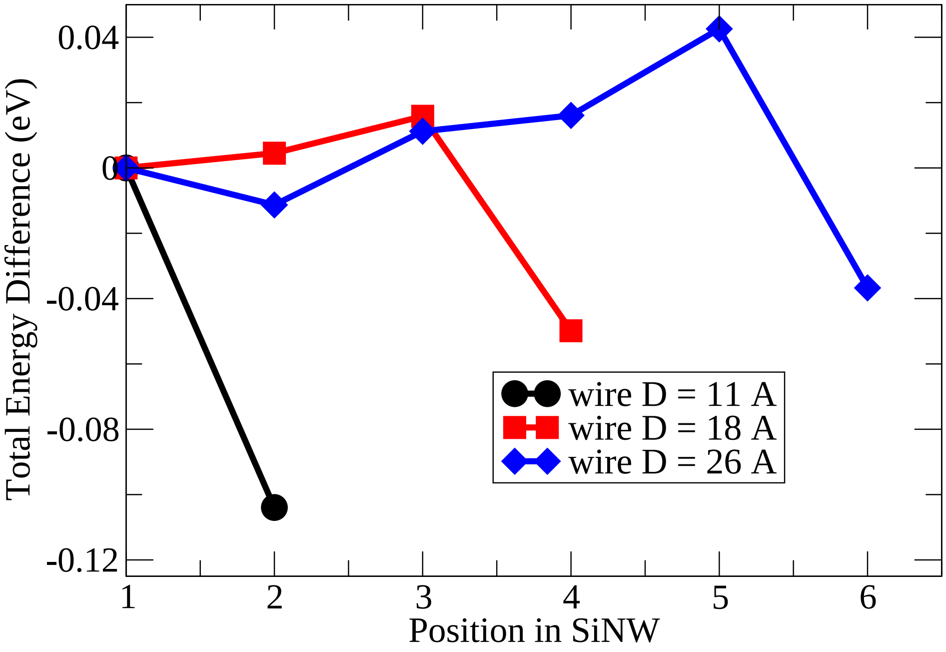

Figure 6.3: Energetics of P atoms in Si ⟨110⟩ nanowires. 1 is the central layer. As one moves a bond length from the center, the numbers increase correspondingly.

6.4 Core-level shift

The core-level binding energy is the difference between the total energies of the system after and before ionization of one core electron. The core-level binding energy shift is just the difference between two core-level binding energies, one of them is a reference we choose. The core-level binding energy shifts are usually observed by X-ray photoelectron spectroscopy (XPS). Here we present two computational methods to calculate the core-level shifts: the initial-state method and the final-state method.

We use 4 smallest cells along wire axis and 8 a.u. vacuum in radial direction as supper cell to relax all the P-doped Si nanowires to their local energy minimum structures. There is only one P atom in each super cell. Only Γ point is calculated. We use 0.4 a.u. as grid spacing.

The final state method for determining the core level shift follows from the definition of the core-level shift and is expressed as

$$E_{core-level}^{shift} = (E_i - E_0) - \left(E_i^{ref} - E_0^{ref}\right), \tag{6.2}$$

where $E_{core-level}^{shift}$ is the core-level shift we want to calculate, E_i and E_0 are the total energies of the system we are interested in after and before ionization of one core electron respectively, E_i^{ref} and E_0^{ref} are the total energies of the reference system after and before the ionization of one core electron respectively.

Two pseudopotentials need to be generated: one is the ordinary atom core pseudopotential that is used to calculate the total energy before ionization. the other is the pseudopotential with one core electron taken out that is used to calculate the total energy after the ionization. In addition there are also two situations that need to be considered: (1) the core electron is taken to the vacuum and no other electron gets into the system, then the system is positive charged; (2) the core electron is taken to the valence band or the core electron is taken to vacuum and some electron from vacuum goes into the valence band, then the system is neutrally charged. When we perform the calculation, some approximations have been made. Relaxation effect of core electron has been neglected, except that we generate two pseudopotentials.

The atomic positions have been frozen, because the XPS event ($10^{-16} sec$) is sudden on the vibration scale ($10^{-13} sec$). In the final-state method, relaxation of the valence electrons has been included.

The results of 2s and 2p core-level shift of P atoms in Si nanowires from final-state method are shown in Fig. 6.4, Fig. 6.5, Fig. 6.6 and Fig. 6.7. From the results, the core-level shifts are bigger when P atoms are closer to the surface of the Si nanowires. The neutral ones have bigger core-level shifts compared to the charged ones.

The initial-state method is based on the first-order perturbation theory. The core-level shifts are the eigenvalues of matrix G. The elements of matrix G for a given angular quantum number l can be expressed as:

$$G^{l}_{m1,m2} = \langle \phi_{l,m1} | V_{scf} - V^{ref}_{scf} | \phi_{l,m2} \rangle. \tag{6.3}$$

where $m1$ and $m2$ are magnetic quantum numbers, $\phi_{l,m1}$ and $\phi_{l,m2}$ are the wave functions of the atom we are interested in with angular quantum number l and magnetic quantum number $m1$ and $m2$ respectively from all-electron calculation for the atom, V_{scf} is the SCF potential of the system we are interested in. V^{ref}_{scf} is the SCF potential of the reference system. When l is not 0, the average of the eigenvalues is calculated as the core-level shift, because the eigenvalues are nearly degenerate. The initial-state method does not include the relaxation of core electrons and valence electrons. The results of 2s and 2p core-level shift of P atoms in Si nanowires from initial-state method are shown in Fig. 6.8 and Fig. 6.9. The results from the initial-state method are

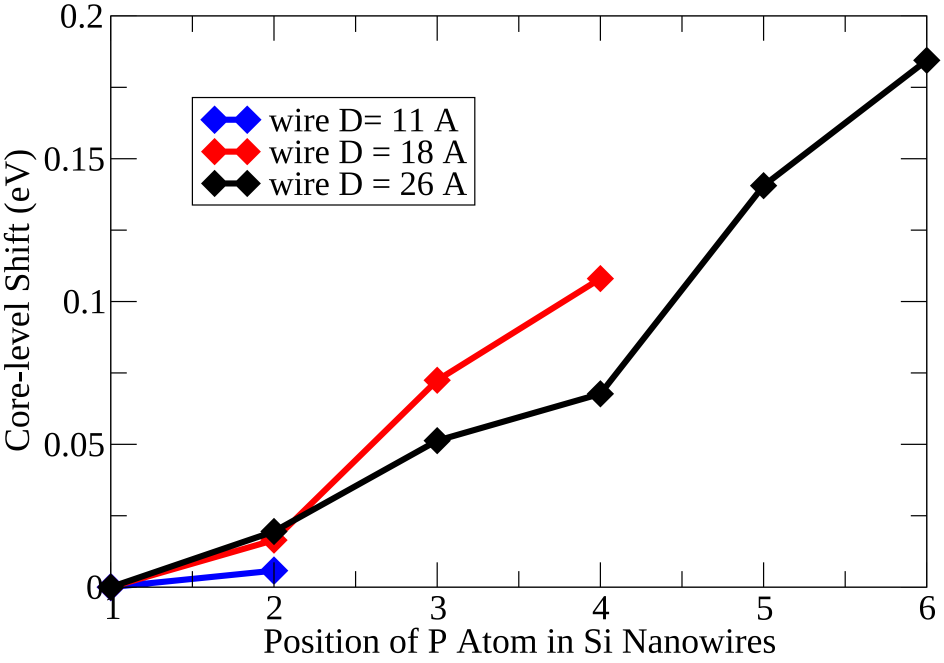

Figure 6.4: Final-state 2s core-level shifts of the P atoms in charged Si $\langle 110 \rangle$ nanowires.

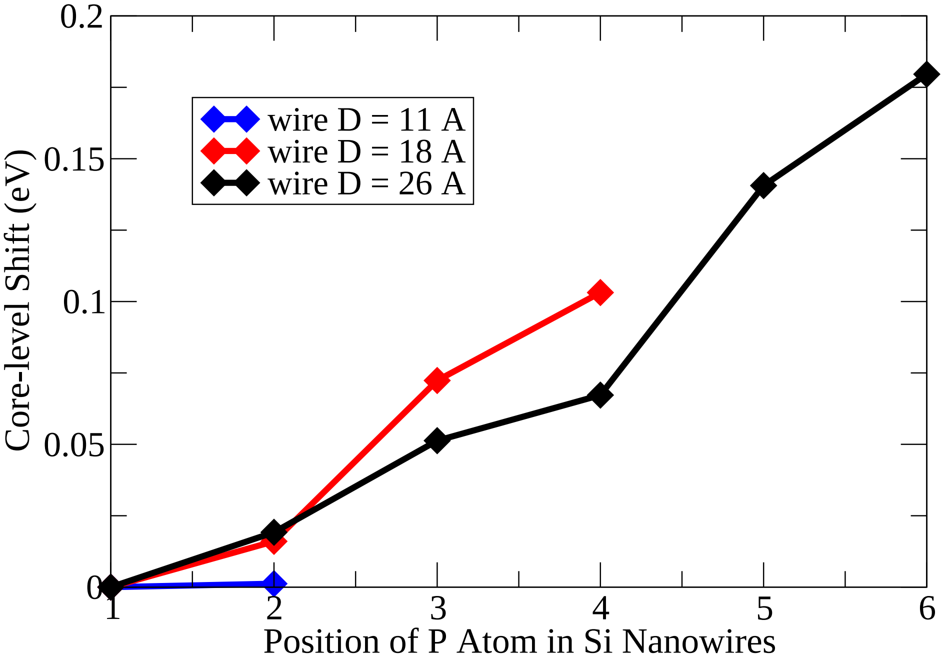

Figure 6.5: Final-state 2p core-level shifts of the P atoms in charged Si $\langle 110 \rangle$ nanowires.

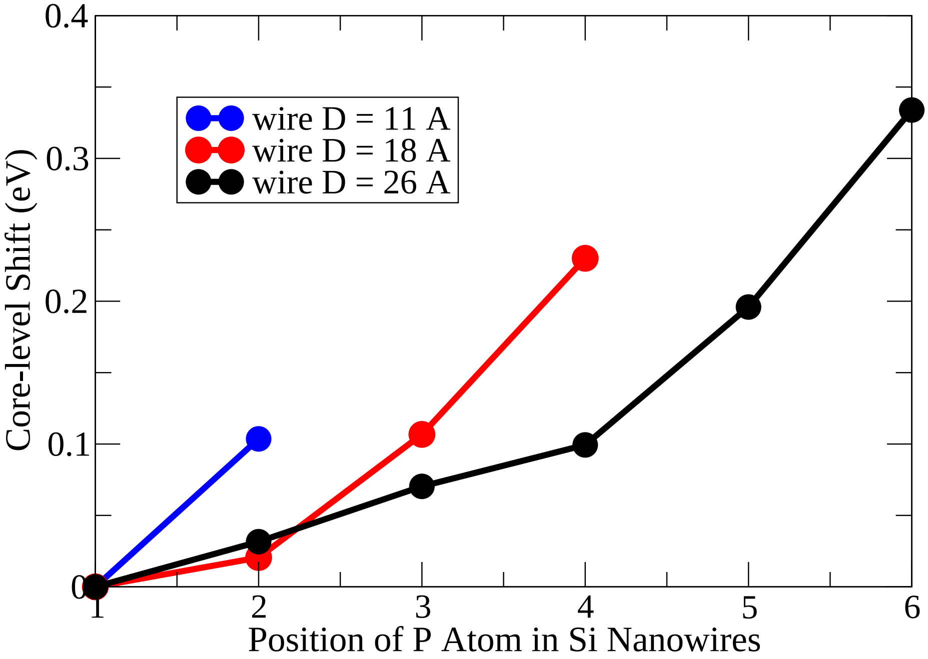

Figure 6.6: Final-state 2s core-level shifts of the P atoms in neutral Si ⟨110⟩ nanowires.

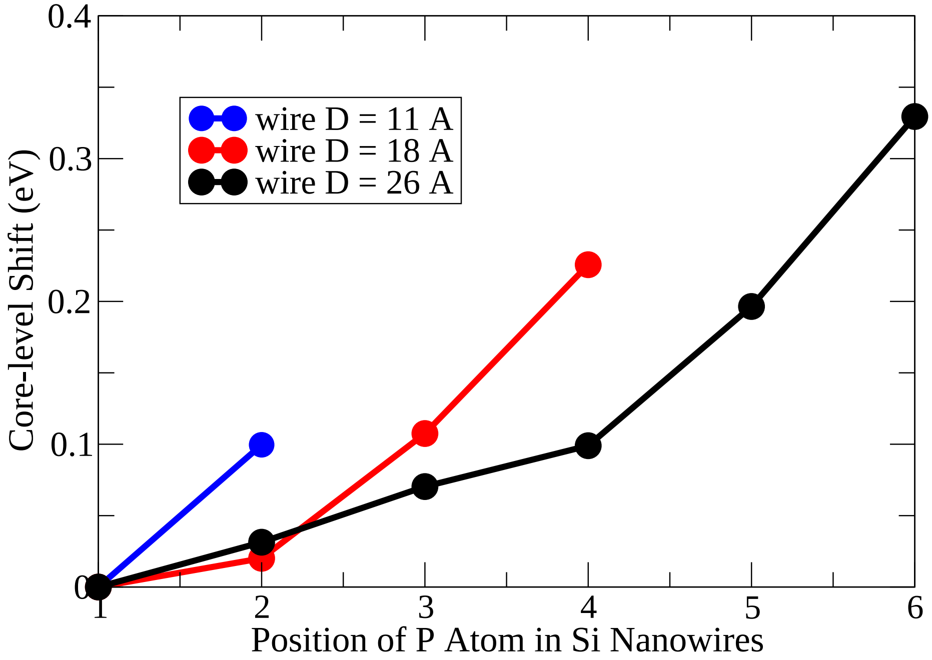

Figure 6.7: Final-state 2p core-level shifts of the P atoms in neutral Si $\langle 110 \rangle$ nanowires.

much smaller compared to the final-state method. The results of 2s are bigger compared to 2p.

6.5 Defect wave functions

Defect wave functions of P atoms in Si nanowires have been analyzed and compared to the Si nano crystals. We chose seven primitive cells along the wire axis and 8 a.u. of vacuum along radial direction as super cells. All P atoms are in the center of the Si nanowires and there is only one P atom in

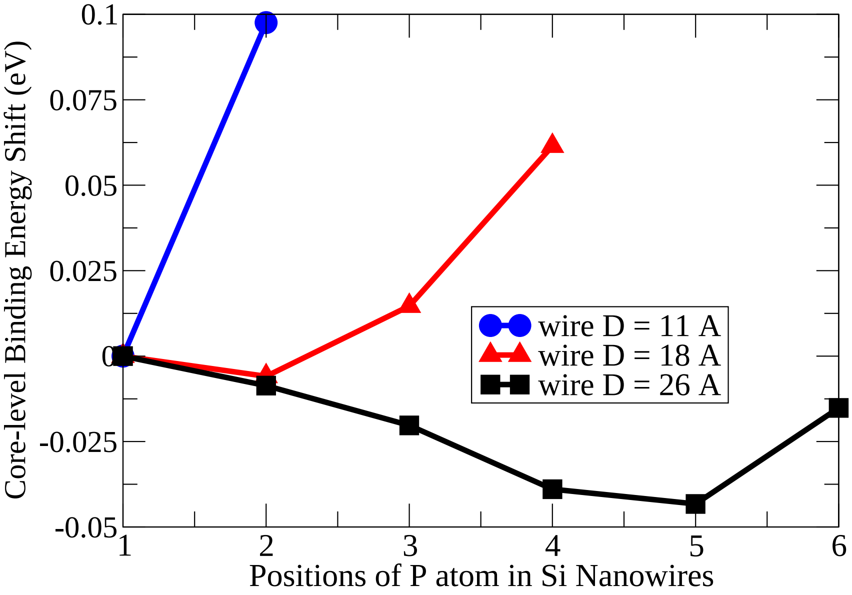

Figure 6.8: Initial-state 2s core-level shifts of the P atoms in neutral Si ⟨110⟩ nanowires.

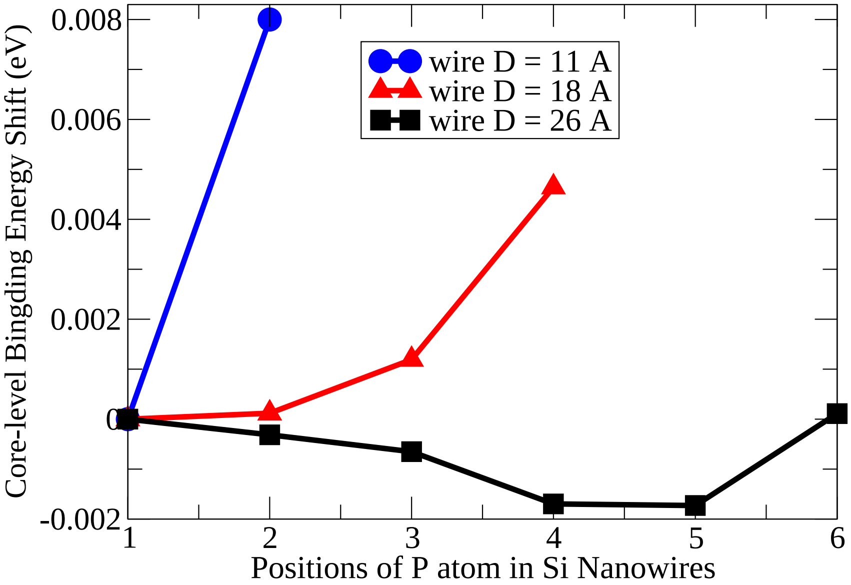

Figure 6.9: Initial-state 2p core-level shifts of the P atoms in neutral Si ⟨110⟩ nanowires.

each super cell. The wave functions are fit to simple functions:

$$\langle\psi_{def}|\psi_{def}\rangle = K\,(x)\,exp\left(-2r/a_B^{eff}\right), \tag{6.4}$$

where x is the coordinate along the wire axis, r is the coordinate along the radial direction, (the origin of the coordinates is the center of the wire where the P atom is), ψ_{def} is the defect wave function, $K\,(x)$ is a function of x and a_B^{eff} is a constant for a given wire, which can be called the effective bohr radius. The results are shown as Fig. 6.10. The effective bohr radius of wires are bigger when the wires' diameters increase. The defect wave function is sphere if there is no confinement. But when there is confinement along two directions, the defect wave function will be deformed and extended along the periodic direction. when the diameter of the wire increases, the confinement effect is weaker, and the deformation is smaller, then the defect wave function will extended more along the confinement direction.

Compared to the nano crystals, the effective bohr radius of wires are slightly smaller, because of the anisotropy of nanowire. The defect wave function is greatly extended along the wire axis, then the radial component ends up decaying faster.

This chapter illustrated a first-principles study of P-doped Si nanowires. We calculated several important quantities in this system and summarize them as below. When the P atom is in the center, the binding energy is bigger for the Si nanowire. The band gap of the Si nanowire increases when the diameter increases. The P atom is more stable on the surface than in the center of the Si nanowires. The center is another stable position for P atom in Si nanowires, when the diameter is larger than 20 Å. In P-doped Si nanowires, the core-level shifts from initial-state method are smaller, compared to final-state method. The core-level binding energy is bigger, when the P atom moves towards the surface. The defect wave functions exponentially decay along the radial direction of P-doped Si nanowires. The effective bohr radius increases when the size of the wire increases.

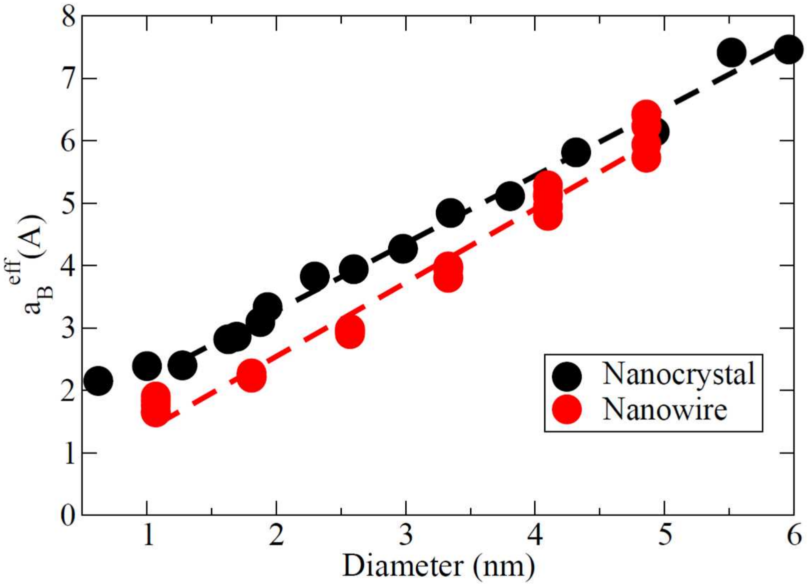

Figure 6.10: Effective bohr radius of defect wave function of the P atoms in Si $\langle 110 \rangle$ nanowire and Si nano crystal.

Chapter 7

P-doped Si $\langle 111 \rangle$ nanofilms and Si-doped GaAs $\langle 110 \rangle$ Nanofilms

7.1 Introduction

Functionalized Si nanofilms have been synthesized and utilized as interconnects in electronic circuits as well as building blocks for semiconductor nanodevices. Likewise, thin films of silicon have been incorporated in transistor applications. For example, microwave thin-film transistors using Si nanomembranes on flexible polymer substrate and microwave thin-film transistors using Si nanomembranes on flexible polymer substrate have been made, and the devices have shown good properties [90,91]. In order to understand how doping operates in these nanostructures, we calculated the properties of the P-doped Si nanofilms. We examine the size dependence of the electronic binding energy for the P donor level in nanofilms as function of size and dimensionality. In particular, we present results for the P doped Si $\langle 111 \rangle$ nanofilms with respect to the film thickness. We also simulate the nanoscale pattern in scanning tunneling microscopy (STM) for Si $\langle 111 \rangle$ nanofilms, and the results agree well with experimental STM images and theoretical calculations by other groups [1,2]. Furthermore,we also study the Si-doped GaAs $\langle 110 \rangle$ nanofilms, and we calculate the binding energies of Si atoms in different depths of the films. Our results show that the binding energy increase when the Si atoms move towards the surface, which agrees well with the experimental measurements [92].

7.2 Methods and calculation details

We studied the pure and P-doped Si $\langle 111 \rangle$ films, which are H-passivated Si $\langle 111 \rangle$ slabs with 3, 5, 7, and 9 double layers of Si atoms. The pure Si nanofilm configuration is illustrated in Fig. 7.1.

The lattice constant used to generate the geometry is the bulk Si lattice constant 5.43 Å, which equals to the experimental measurement. A 6×6 unitcell and 20 a.u. vacuum space are used to perform the calculation. The gridspacing used is 0.5 a.u..

Here we use the slab boundary conditions embedded in PARSEC package [14] using a new generalized high-order finite-difference algorithm. The slab boundary condition is two-dimensional periodic boundary condition, which is periodic along x and y directions and confined in the z direction.

The wave-functions $\psi_i(\mathbf{r})$ with energy E_i can be computed using real space pseudopotential density functional theory method described above. The STM tunneling current $j(\mathbf{r})$ can be computed approximately [93] using

$$j(\mathbf{r}) \sim \int_{E_f}^{E_f - eV} \rho(\mathbf{r}, E) dE \tag{7.1}$$

where

$$\rho(\mathbf{r}, E) = \sum_i |\psi_i(\mathbf{r})|^2 \, \delta(E_i - E) \tag{7.2}$$

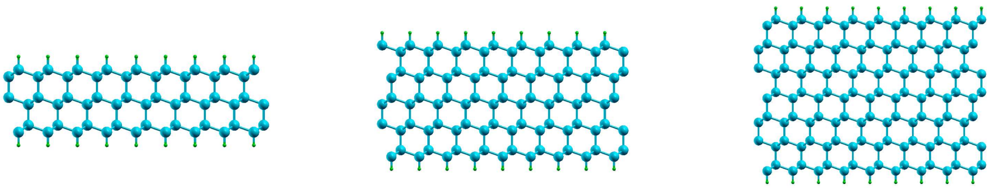

(a) 3 layers side view (b) 5 layers side view (c) 7 layers side view

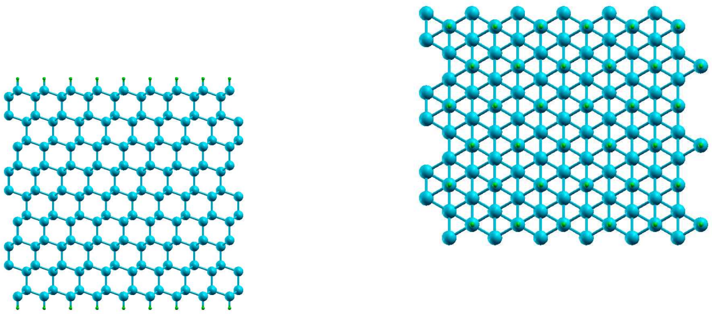

(d) 9 layers side view (e) 6 x 6 unit cell xy-plane top view

Figure 7.1: Side view and top view of pure H-passivated Si $\langle 111 \rangle$ nanofilms of different thickness. The blue spheres correspond to Si atoms, and the green smaller spheres on the surface of the nanofilm are H atoms.

$\rho(\mathbf{r}, E)$ is the local density of states at the STM tip position. E_f is the Fermi energy, and V is the STM tip bias voltage.

7.3 Doping phosphorus into Si nanofilms

The band gaps of pure Si $\langle 111 \rangle$ films of different thickness have been calculated. The HOMO-LUMO gap, which is defined as the energy difference between the conduction band minimum and valence band maximum is illustrated in Fig.7.3. For the pure Si $\langle 111 \rangle$ films, the gap decreases when the film is thicker. The gap will converge to the bulk value of the Si, which is 0.64 eV.

The configurations of P-doped Si $\langle 111 \rangle$ films with P atoms in the central layers are shown in Fig. 7.2. The binding energy, the energetics of P atoms in P-doped Si $\langle 111 \rangle$ films are investigated. When P atoms are in the central layers, the binding energy decreases with increased thickness, as plotted in Fig. 7.4. The binding energy is calculated using the energy spectrum. The binding energy is evaluated by subtracting defect level from conduction band minimum of pure Si films.

One of the fundamental questions for doped semiconductors is where is the most stable position for the doped atoms. We investigate the energetics of the P atom sites in the Si $\langle 111 \rangle$ film by calculating the relative energies of different substitutional sites. We calculated the relative energies of P-doped Si $\langle 111 \rangle$ films with P in different depths of the films. We consider films of 5, 7 and 9 double layers as illustrated in Fig. 7.5. We found that the central layers are the most energetically favorable positions for P atoms.

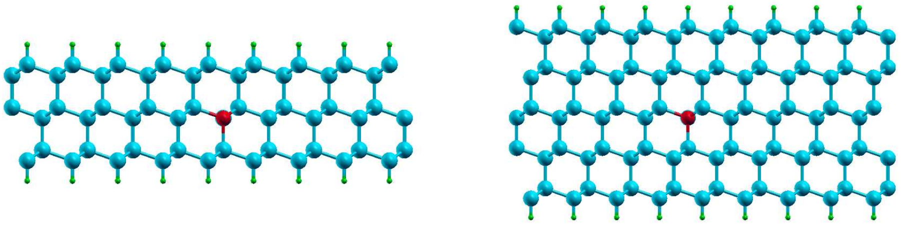

(a) 3 layers

(b) 5 layers

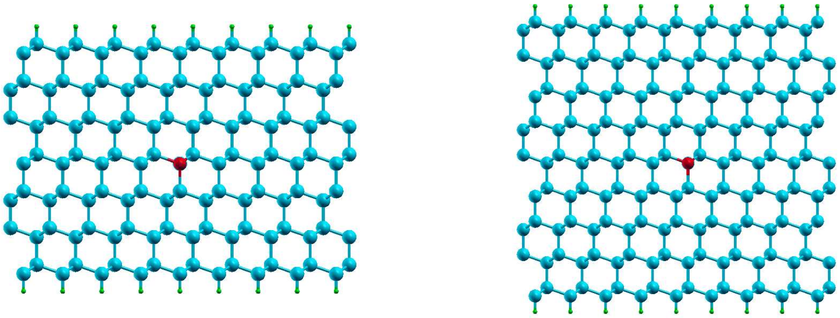

(c) 7 layers

(d) 9 layers

Figure 7.2: Side view of P-doped H-passivated Si $\langle 111 \rangle$ nanofilms of different thickness, with P atoms in the central layers. The blue spheres correspond to Si atoms, and the green smaller spheres on the surface of the nanofilms are H atoms. The red ones are the doped P atoms.

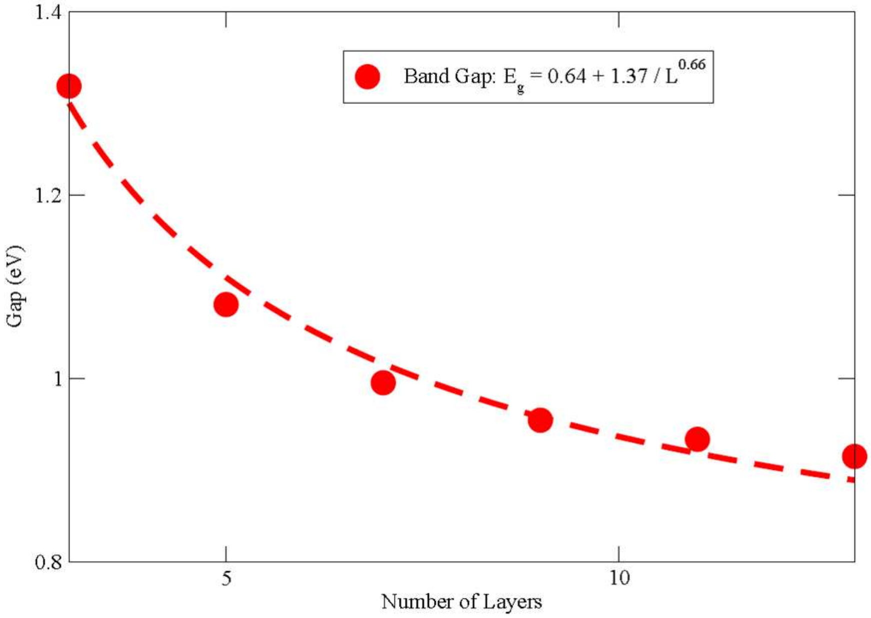

Figure 7.3: Band gap of pure Si ⟨111⟩ nanofilm.

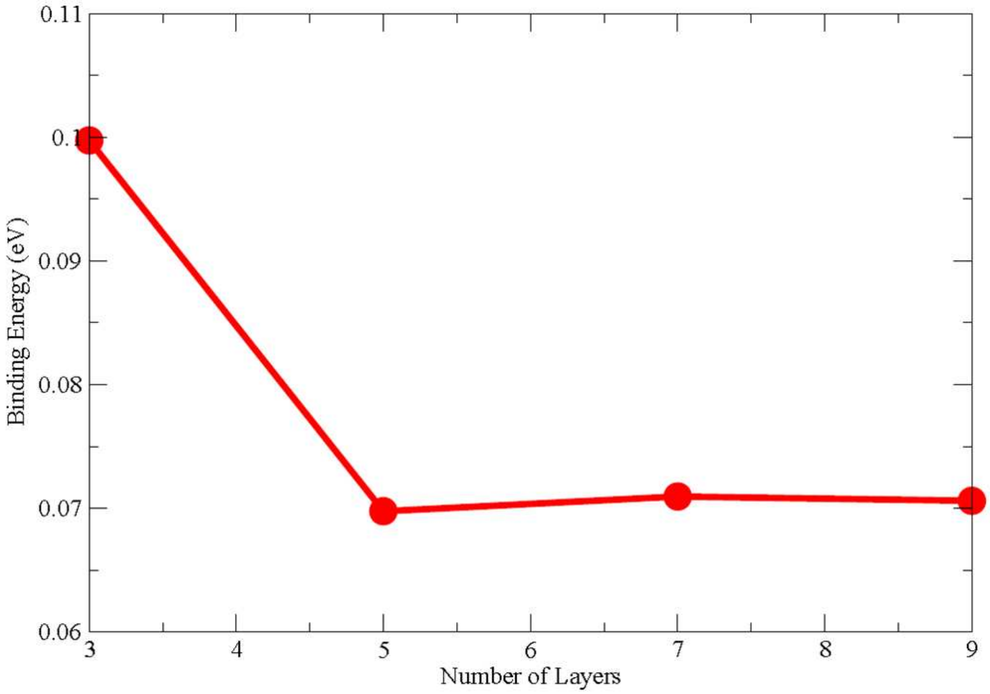

Figure 7.4: Binding energy of P atoms in P-doped Si ⟨111⟩ nanofilms with different thickness. All the P atoms are in the central layers.

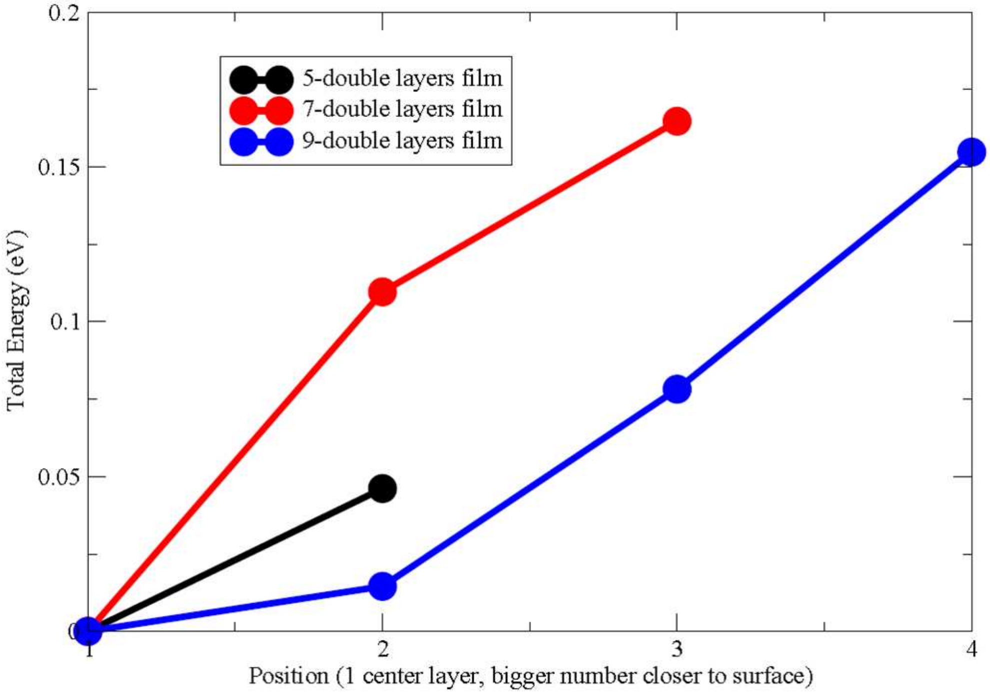

Figure 7.5: Energetics of P atoms in P-doped Si $\langle 111 \rangle$ films. The energies are relative total energies, and the x-axis indicates the position of the dopant (1 is the central layer. As one moves a bond length from the center, the numbers increase correspondingly.)

In experiments, when STM is in the constant current mode, the tip follows a contour of a constant tunneling current during scanning. Since the current is proportional to the local density of states, we effectively follow the contour of the constant local density states during scanning. A kind of a topographic image of the surface is generated by recording the vertical position of the tip.

We simulated the STM images of P-doped Si $\langle 111 \rangle$ films with different bias voltages and different P positions. The tunneling current in STM is proportional to the integration of the charge densities from the Fermi energy to Fermi energy plus the bias voltage. The constant current mode of STM was simulated, and the vertical positions of the tip with the same local density of states was recorded in the simulated STM images.

In the simulated STM images, the contrast reverses when the bias voltage changes the sign. The P site is darker than background when bias voltage is negative. The P site is brighter than background when bias voltage is positive. Our calculations are illustrated in Fig. 7.6. These results agree well with experiments and calculations from another group [1, 2].

We also calculated the STM images with P atoms in different layers of the Si $\langle 111 \rangle$ nanofilms. The results are illustrated in Fig. 7.7. It is clear that when P atoms are in the deeper layer of Si $\langle 111 \rangle$ films, the STM feature of P site is larger .

7.4 Doping silicon into GaAs nanofilms

The binding energies of Si atoms in GaAs $\langle 110 \rangle$ films have been experimentally studied when the Si atoms move to the surface [92]. In this work, we calculate the binding energy of Si atoms in different depths of 5 double-layered GaAs $\langle 110 \rangle$ films using 5 x 5 unit cell on the surface shown in Fig. 7.8. The results are illustrated in Fig. 7.8(b), and a comparison is made to experimental data 7.8(c). When the Si atoms move towards surface, the binding energy increases. This agrees with experiment.

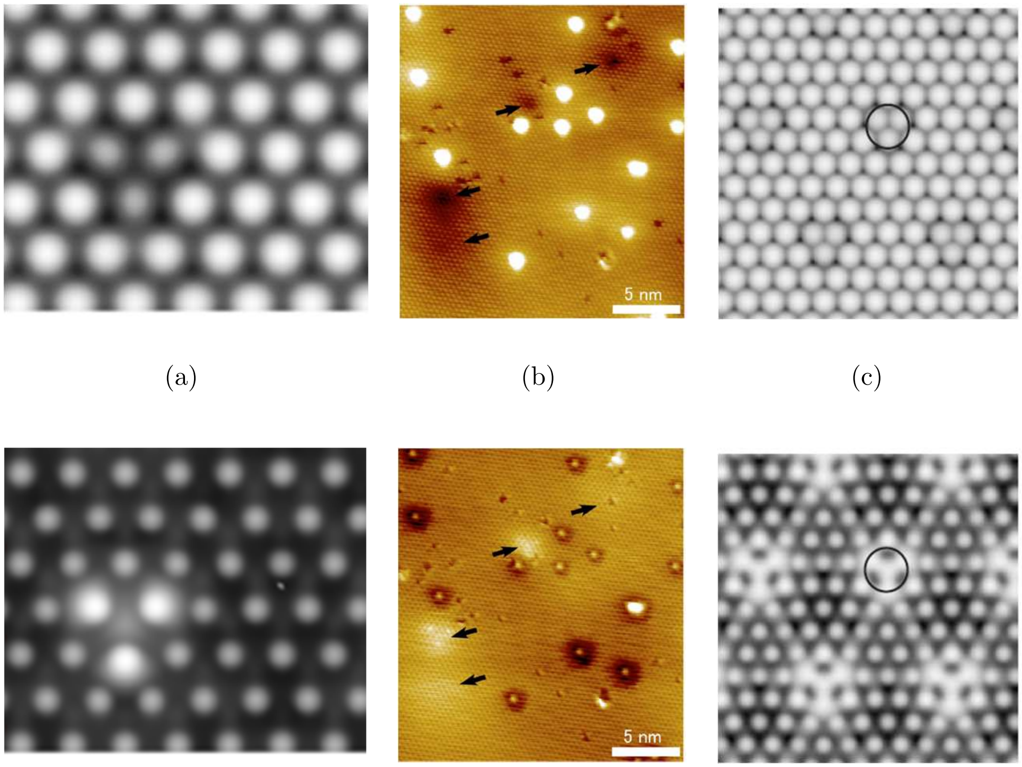

(a) (b) (c)

(d) (e) (f)

Figure 7.6: Simulated STM images of P-doped Si ⟨111⟩ nanofilms compared with experimental data by Nishizawa et al. [1] and theoretical calculation by Hirayama et al. [2]. Simulated STM image with P in the first layer when bias voltage equals 1V (a) and -3V (d). Experimental STM images when bias voltage equals -1.5V, tunneling current equals 0.1 nA (b) and when bias voltage equals +1V, tunneling current equals 0.1 nA (e). Calculated STM images with P in the first layer when bias voltage equals -3V (c) and when bias voltage equals 2V (f).

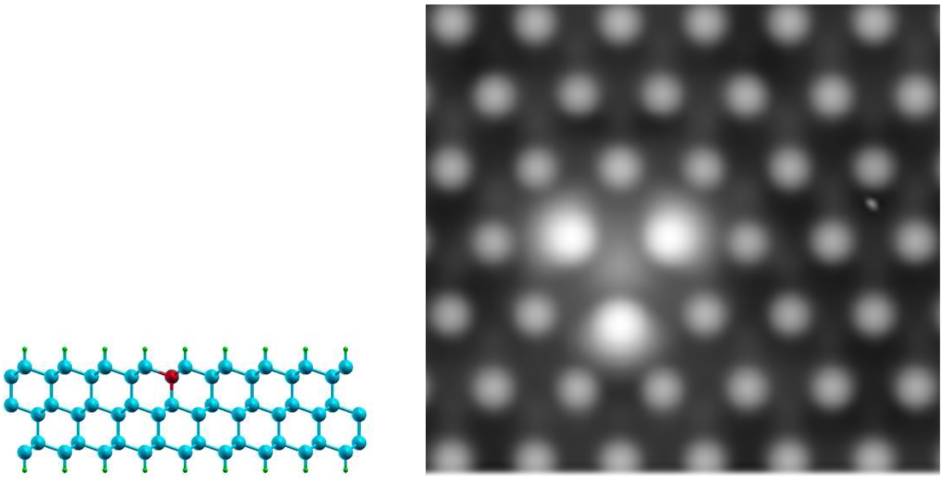

(a) Configuration of the film when P is in the first layer

(b) Simulated STM images when P is in the first layer and bias voltage is 1V

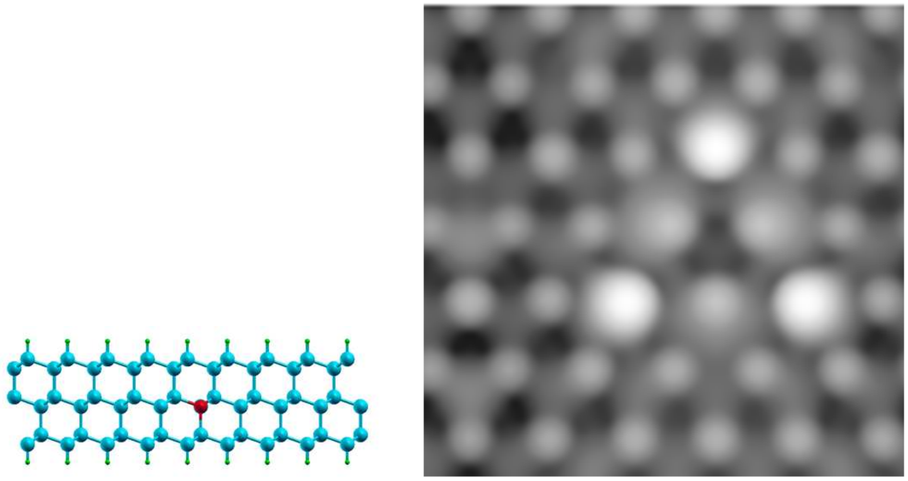

(c) Configuration of the film when P is in the second layer

(d) Simulated STM images when P is in the second layer and bias voltage is 0.5V

Figure 7.7: Simulated STM images of P-doped Si ⟨111⟩ nanofilms with different depths.

We employed a real-space pseudopotential method to study P-doped Si nanofilms and Si-doped GaAs nanofilms. For pure Si $\langle 111 \rangle$ nanofilm, the results of band gap shows the quantum confinement effects. For the P-doped Si $\langle 111 \rangle$ nanofilms, the results of binding energy and energetics are presented. The binding energy decreases when the thickness of the film increases. The most stable dopant positions are obtained to be the central layers of the films. The nanoscale pattern in STM for P-doped Si $\langle 111 \rangle$ films are simulated, and the results agree well with experimental STM images and theoretical calculations by other groups [1, 2].

Effective mass theory of Coulomb impurities predicts a reduction of E_b close to a barrier [94]. However, for low dimensional systems an enhancement is expected, as was shown by the tight binding method for quantum rods [95] and by density functional theory (DFT) calculations for nanocrystals [89].

For 5 double-layered GaAs $\langle 110 \rangle$ films, our results demonstrated that the binding energy increase when the Si atoms move towards the surface. Measurements for the electronic structure of these dopants are reproduced by our calculations [92].

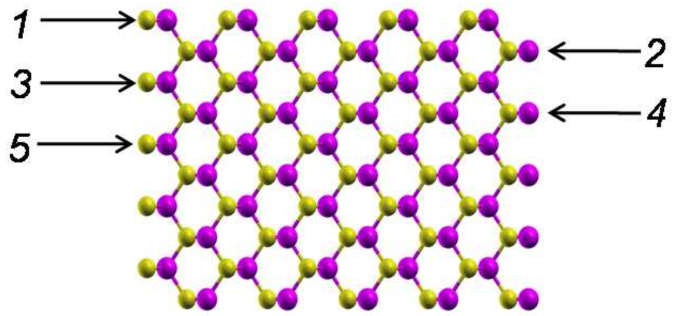

(a) Schematic diagrams illustrating the position of Si atoms in different depths of 5 double-layered GaAs $\langle 110 \rangle$ films.

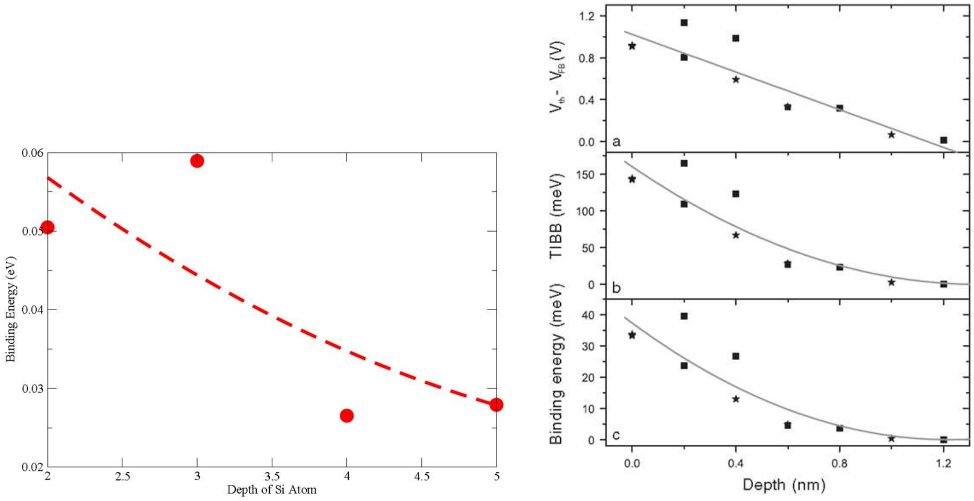

(b) The binding energy of Si atoms in different depths of 5 double-layered GaAs $\langle 110 \rangle$ films calculated using real-space pseudopotential method (our work). The dash line is added to guide the eye.

(c) The estimated binding energy of Si atoms in GaAs surfaces in subfig c taken from literature [92]. The solid lines are added to guide the eye.

Figure 7.8: Comparison of the binding energy of Si atoms in GaAs $\langle 110 \rangle$ films.

Bibliography

[1] M. Nishizawa, L. Bolotov, T. Tada, and T. Kanayama. *J. Vac. Sci. Technol. B.*, 24:365, 2006.

[2] M. Hirayama, J. Nakamura, and A. Natori. *Jpn. J. Appl. Phys.*, 46:5643, 2007.

[3] Y. Cui, Z. Zhang, D. Wang, W. U. Wang, and C. M. Lieber. *Nano Lett.*, 3:149, 2003.

[4] Y. Huang, X. Duan, Y. Cui, L. J. Lauhon, K. Kim, and C. M. Lieber. *Science*, 294:1313, 2001.

[5] X. Wang, J. Song, J. Liu, and Z. L. Wang. *Science*, 316:102, 2007.

[6] W. Lu and C. M. Lieber. *J. Phys. D: Appl. Phys.*, 39:R387, 2006.

[7] Y. Cui, Q. Wei, H. Park, and C. M. Lieber. *Science*, 293:1289, 2001.

[8] F. Patolsky, G. Zheng, and C. M. Lieber. *Analytical Chemistry*, 4261, 2006.

[9] G. Gamov. *Thirty Years That Shook Physics: The Story of Quantum Theory.* Dover, New York, 1966.

[10] E. Fermi. *Nuovo Cimento*, 11:157, 1934.

[11] N. D. M. Hine, K. Frensch, W. M. C. Foulkes, and M. W. Finnis. *Phys. Rev. B.*, 79:024112, 2009.

[12] A. S. Foster, V. B. Sulimov, F. Lopez Gejo, A. L. Shluger, and R. M. Nieminen. *Phys. Rev. B.*, 64:224108, 2001.

[13] M. M. G. Alemany, M. Jain, M. L. Tiago, Y. Zhou, Y. Saad, and J. R. Chelikowsky. *Comp. Phys. Commun.*, 177:339, 2007.

[14] A. Natan, A. Benjamini, D. Naveh, L. Kronik, M. L. Tiago, S. Beckman, and J. R. Chelikowsky. *Phys. Rev. B*, 78:075109, 2008.

[15] J. R. Chelikowsky, S Y. Saad, I. Vasiliev Öğüt, and A. Stathopoulos. *Phys. Stat. Solidi B-Basic Research*, 217:173, 2000.

[16] L. Kong, M. L. Tiago, and J. R. Chelikowsky. *Phys. Rev. B*, 73:195118, 2006.

[17] J. Han, M. L. Tiago, T.-L. Chan, and J. R. Chelikowsky. *J. Chem. Phys.*, 129:144129, 2008.

[18] S. P. Beckman, J. Han, and J. R. Chelikowsky. *Phys. Rev. B*, 74:165314, 2006.

[19] G. Zheng, W. Lu, S. Jin, and C. M. Lieber. *Adv. Mater.*, 16:1890, 2006.

[20] G. Zheng, F. Patolsky, Y. Cui, W. U. Wang, and C. M. Lieber. *Nature Biotechnology*, 23:1294, 2005.

[21] E. Durgun, N. Akman, C. Ataca, and S. Ciraci. *Phys. Rev. B.*, 76:245323, 2007.

[22] J. R. Chelikowsky and M. L. Cohen. *Ab Initio Pseudopotentials for Semiconductors*, volume 1 of *Handbook on Semiconductors*, page 59. Amsterdam: Elsevier, 1992.

[23] J. R. Chelikowsky. *J. Phys. D*, 33:R33, 2000.

[24] L. Kronik J. R. Chelikowsky and I. Vasiliev. *J. Phys. Condens. Matter*, 15:R1517, 2003.

[25] J. R. Chelikowsky and Y. Saad. *Electronic structure of clusters and nanocrystals. Handbook of Theoretical and Computational Nanotechnology.* American Scientific, 2006.

[26] J. R. Chelikowsky Y. Saad and S. M. Shontz. *SIAM Review*, 52:3, 2010.

[27] M. Born and R. Oppenheimer. *Ann. d. Physik.*, 84:457, 1927.

[28] P. Hohenberg and W. Kohn. *Phys. Rev. B*, 136:864, 1964.

[29] W. Kohn and L. J. Sham. *Phys. Rev. A*, 140:1133, 1965.

[30] J. C. Phillips and L. Kleinman. *Phys. Rev.*, 116:287, 1959.

[31] J. R. Chelikowsky, N. Troullier, and Y. Saad. *Phys. Rev. Lett.*, 72:1240, 1994.

[32] Y. Zhou, Y. Saad, M. L. Tiago, and J. R. Chelikowsky. *J. Comput. Phys.*, 219:172, 2006.

[33] Y. Zhou, Y. Saad, M. L. Tiago, and J. R. Chelikowsky. *Phys. Rev. E*, 74:066704, 2006.

[34] J. M. Ziman. *Electrons and Phonons.* Oxford University Press, Oxford, 1960.

[35] A. Haug. *Theoretical Solid State Physics.* Pergamon Press, Oxford, 1972.

[36] D. C. Langreth and J. P. Perdew. *Phys. Rev. B*, 21:5469, 1980.

[37] D. C. Langreth and M. J. Mehl. *Phys. Rev. B*, 28:1809, 1983.

[38] V. N. Staroverov J. Tao, J. P. Perdew and G. E. Scuseria. *Phys. Rev. Lett.*, 91:146401, 2003.

[39] W. Kohn and L. J. Sham. *Phys. Rev.*, 140:A1133, 1965.

[40] D. M. Ceperley and B. J. Alder. *Phys. Rev. Lett.*, 45:566, 1980.

[41] J. P. Perdew and A. Zunger. *Phys. Rev. B*, 23:5048, 1981.

[42] M. L. Cohen and J. R. Chelikowsky. *Electronic structure and optical properties of semiconductors.* Springer-Verlag, New York, 1988.

[43] M. L. Cohen and J. R. Chelikowsky. *Pseudopotentials for Semiconductors*, volume 1 of *Handbook on Semiconductors.* Amsterdam: North Holland.

[44] G. P. Kerker. *J. Phys. C*, 13:L189, 1980.

[45] D. R. Hamann, M. Schlüter, and C. Chiang. *Phys. Rev. Lett.*, 43:1494, 1979.

[46] G. B. Bachelet, D. R. Hamann, and M. Schlüter. *Phys. Rev. B*, 26:4199, 1982.

[47] H. S. Greenside and M. Schlüter. *Phys. Rev. B*, 26:4199, 1983.

[48] L. Kleinman and D. M. Bylander. *Phys. Rev. Lett.*, 48:1425, 1982.

[49] N. Troullier and J. L. Martins. *Phys. Rev. B*, 43:1993, 1991.

[50] J. L. Martins N. Binggeli and J. R. Chelikowsky. *Phys. Rev. Lett.*, 68:2956, 1992.

[51] C.G.Van de Walle and D. Bar-Yam. *Phys. Rev. B.*, 39:10791, 1989.

[52] M. C. Payne, M. P. Teter, D. C. Allan, T. A. Arias, and J. D. Joannopoulous. *Rev. of Mod. Phys.*, 64:1045, 1992.

[53] D. Jackson. *Classical Electrodynamics.* Wiley, 1992.

[54] D. Smith. *Numerical Solutions of Partial Differential Equations: Finite Difference Methods, Second Ed.* Oxford, New York, 1978.

[55] B. Fornberg and D. M. Sloan. *Acta Numer.*, 94:203, 1994.

[56] J. R. Chelikowsky, M. L. Tiago, Y. Saad, and Y. Zhou. *Comp. Phys. Commun.*, 177:1, 2007.

[57] http://parsec.ices.utexas.edu.

[58] M. Abramowitz and I. A. Stegun. *Handbook of Mathematical Functions: with Formulas, Graphs, and Mathematical Tables.* Dover, 1965.

[59] A. Arnold and C. Holm. *J. Chem. Phys.*, 123:144103, 2005.

[60] J. Ihm, A. Zunger, and M. L. Cohen. *J. Phys. C: Solid State Phys.*, 12:4409, 1979.

[61] M. Fujii, Y. Yamaguchi, Y. Takase, K. Ninomiya, and S. Hayashi. *Appl. Phys. Lett.*, 85:1158, 2004.

[62] M. Fujii, Y. Yamaguchi, Y. Takase, K. Ninomiya, and S. Hayashi. *Appl. Phys. Lett.*, 87:211919, 2005.

[63] M. Tan, V. Mahalingam, and F. C. J. M. van Veggel. *Appl. Phys. Lett.*, 91:093132, 2007.

[64] J. D. Holmes, K. P. Johnston, R. C. Doty, and B. A. Korgel. *Science*, 287:1471, 2000.

[65] B. V. Kamenev, V. Sharma, L. Tsybeskov, and Kamins T. I. *Phys. Status Solidi A*, 202:2753, 2005.

[66] G. Jin, Y. S. Tang, J. L. Liu, and K. L. Wang. *J. Vac. Sci. Technol. A*, 17:1406, 1999.

[67] G. Audoit, E. Mhuircheartaigh, S. M. Lipson, M. A. Morris, W. J. Blau, and J. D. Holmes. *J. Mater. Chem.*, 15:4809, 2005.

[68] I. Vasiliev, S. Ogut, and J. R. Chelikowsky. *Phys. Rev. B*, 65:115416, 2002.

[69] I. Vasiliev, S. Ogut, and J. R. Chelikowsky. *Phys. Rev. Lett.*, 86:1813, 2001.

[70] I. Vasiliev, S. Ogut, and J. R. Chelikowsky. *Phys. Rev. B*, 60:R8477, 1999.

[71] S. Ogut, J. R. Chelikowsky, and S. G. Louie. *Phys. Rev. Lett.*, 79:1770, 1997.

[72] X. Zhao, C. M. Wei, L. Yang, and M. Y. Chou. *Phys. Rev. Lett.*, 92:236805, 2004.

[73] A. N. Kholod, V. L. Shaposhnikov, N. Sobolev, V. E. Borisenko, F. A. DÁvitaya FA, and S. Ossicini. *Phys. Rev. B*, 7:035317, 2004.

[74] M. Bruno, M. Palummo, A. Marini, R. Del Sole, V. Olevano, A. N. Kholod, and S. Ossicini. *Phys. Rev. B*, 72:153310, 2005.

[75] X. Gonze, J.-M. Beuken, R. Caracas, F. Detraux, M. Fuchs, G.-M. Rignanese, L. Sindic, M. Verstraete, G. Zerah, F. Jollet, M. Torrent, A. Roy,

M. Mikami, Ph. Ghosez, J.-Y. Raty, and D. C. Allan. *Comput. Mater. Sci.*, 25:478, 2002.

[76] J. P. Perdew and Alex Zunger. *Phys. Rev. B*, 23:5048, 1992.

[77] S. G. Louie, S. Froyen, and M. L. Cohen. *Phys. Rev. B*, 26:1738, 1982.

[78] O. Madelung, editor. Data in Science and Technology. Springer-Verlag, New York, 1991.

[79] W. L. Bond, W. P. Mason, H. J. McSkimin, K. M. Olsen, and G. K. Teal. *Phys. Rev.*, 78:176, 1950.

[80] T. L Chan, C. V. Ciobanu, F. C. Chuang, N. Lu, C. Z. Wang, and K. M. Ho. *Nano Lett.*, 6(2):277, 2006.

[81] Y. Wu, Y. Cui, L. Huynh, C. J. Barrelet, D. C. Bell, and C. M. Lieber. *Nano Lett.*, 4(3):433, 2004.

[82] A. J.R. da Silva. *Unpublished data.*

[83] M. S. Hybertsen and S. G. Louie. *Phys. Rev. B.*, 34:5390, 1986.

[84] N. Troullier and J. L. Martins. *Phys. Rev. B*, 43:1993, 1991.

[85] X. Zhao, C. M. Wei, L. Yang, and M. Y. Chou. *Phys. Rev. Lett.*, 92:236805, 2004.

[86] S. Lundqvist and N. H. March. *Theory of the Inhomogeneous Electron Gas*, 1983.

[87] B. Streetman and Sanjay Banerjee. *Solid State electronic Devices (5th ed.)*, 2000.

[88] P. Aigrain and M. Balkanski. *Selected Constants Relative to Semiconductors*, 1961.

[89] T.-L. Chan, M. L. Tiago, E. Kaxiras, and J. R. Chelikowsky. *Nano Lett.*, 8:596, 2008.

[90] J.-H. Ahn, H.-S. Kim, Z. Zhu K. J. Lee, E. Menard, R. G. Nuzzo, and J. A. Rogers. *IEEE Elect. Dev. Lett.*, 27:6, 2006.

[91] H.-C. Yuan, Z. Ma, M. M. Roberts, D. E. Savage, , and M. G. Lagally. *J. Appl. Phys.*, 100:013708, 2006.

[92] A. P. Wijnheijmer, J.K. Garleff, K. Teichmann, M. Wenderoth, S. Loth, R.G. Ulbrich, P.A. Maksym, M. Roy, and P. M. Koenradd. *Phys. Rev. Lett.*, 102:166101, 2009.

[93] J. Tersoff and D. R. Hamann. *Phys. Rev. B*, 31:805, 1985.

[94] G. Bastard. *Wave Mechanics Applied to Semiconductor Heterostructures*, 1988.

[95] M. Diarra, Y. M. Niquet, C. Delerue, and G. Allan. *Phys. Rev. B*, 75:045301, 2007.

Vita

Jiaxin Han was born in Inner-Mongolia in China. He received the Bachelor of Science degree in Physics from the University of Science and Technology of China in 2004. He came to the United States and entered the University of the University of Texas at Austin in August of 2004.

Permanent address: 2501 Lake Austin Blvd N204
Austin, Texas 78703

This dissertation was typeset with LaTeX[†] by the author.

[†] LaTeX is a document preparation system developed by Leslie Lamport as a special version of Donald Knuth's TeX Program.